

Chapter 1

Fundamentals of Nucleation Theory

Theoretical analysis of nucleation rates and distributions of nuclei over sizes is of great importance in connection with clustering and condensation in vapors, crystallization of liquid alloys, phase separation in solid solutions, kinetics of colloidal and biological systems and many other growth-related phenomena such as thin film condensation, epitaxy of semiconductor quantum dots and freestanding nanowires. This chapter gives a systematic introduction to the classical nucleation theory treating the kinetics of phase transition as a spontaneous birth and follow-up growth of embryos in a metastable environment. Below in this book, we will consider both three-dimensional (3D) and two-dimensional (2D) systems or even their combinations such as 3D surface islands growing from a 2D environment. To account for different system configurations, we formulate all necessary expressions in arbitrary dimension $d = 2$ or 3 .

The core assumptions of classical approach are: (i) low enough temperature below T_c and (ii) low enough supersaturation of a metastable phase. The entire system can then be subdivided into an ensemble of dense nuclei and a dilute, almost perfect vapor. The nuclei of interest contain many monomers and are separated from vapor by distinct interfacial boundaries that can be described by macroscopic surface energies. However, the applicability of classical nucleation theory is not always guaranteed, and non-classical scenarios are often observed. To give a feeling of how different these scenarios might be, we start with a detailed analysis of phase transition thermodynamics, presented in Sect. 1.1 in the frame of the lattice gas model. The model is relevant for 3D vapor–liquid phase transitions and is especially well justified for island nucleation on solid surfaces. The equation of state is obtained directly from the statistical sum within the frame of mean field approximation and used for the description of phase equilibrium. Different forms of the equation of state such as chemical potential—density, pressure–volume or magnetization—external field isotherms are discussed. Although not within the scope of our study, we mention the critical phenomena and critical scaling which the mean field theory fails to describe correctly. Section 1.2 presents a classification of the phase transition pathways and relevant theoretical methods of their description, either in terms of size and number of nuclei

or by means of field theories for a fluctuational order parameter. We also show how the central notions of classical nucleation theory such as supersaturation are derived from the mean field equation of state when the temperature is well below the critical value.

In Sect. 1.3, we consider the Laplacian pressure and the corresponding Gibbs–Thomson modification of chemical potential in the nanoparticles, caused by the curvature of their surface. It is this effect which is responsible for the barrier character of nucleation leading to irreversible first order phase transition. On the other hand, the Gibbs–Thomson effect has a tremendous importance in the “vapor–liquid–solid” growth of nanowires, one of the major applications considered later. Section 1.4 might look trivial at first glance, as it studies the well-known Young’s condition for the contact angle of a droplet resting on a solid surface. We show, however, that the usual mechanical balance of the surfaces forces acting upon the triple phase line is not sufficient for stable equilibrium. A remarkable example is given by a spherical droplet seated on top of a cylindrical nanowire. When the droplet slides down along the nanowire sidewalls, the Young’s angle yields the balance of forces but corresponds to the maximum rather than the minimum surface energy!

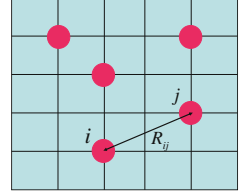
The most important thermodynamic characteristic of any condensing system, the macroscopic formation energy of a nucleus containing i monomers at a given supersaturation, is considered in Sect. 1.5. We discuss different cases such as droplets and crystal nuclei in gas-vapor environments, 2D and 3D surface islands growing on similar and dissimilar substrates, as well as heterogeneous nucleation on condensation seeds. The nucleation barrier and the number of monomers in the critical nucleus are then obtained in arbitrary space dimension. We only briefly analyze the known renormalizations of quasi-equilibrium distribution since, in open systems, the normalization can be obtained in a self-consistent manner. Section 1.6 contains an overview of useful results regarding the adsorption isotherms and thin films on solid surfaces. In particular, we discuss the elementary processes such as adsorption, desorption and surface diffusion, as well as thin film growth either by step flow or islanding. Section 1.7 is very important, as it presents systematization of the known growth scenarios for super-critical nuclei in different systems: surface layers, droplets and islands in different metastable environments. We show that, in most cases, the growth rate is a power law function of the number of monomers with the corresponding index ranging from zero to one. This feature is of fundamental importance for constructing the analytical approximations for the nucleation probabilities and the size spectra.

Finite difference rate equations of nucleation theory in the monomolecular reaction schemes are given in Sect. 1.8. From the very beginning, we consider the open systems where the monomers are delivered by a material influx from a surrounding and monomer sinks are also possible. In the open systems studied below in this book, supersaturation changes in time due to the monomer consumption by the growing nuclei and the material influx, the so-called nucleation under dynamical conditions. This is the major difference of our approach (which, for example, is essential in studying the epitaxy of nanostructures) from those considering the nucleation which originates from a fixed supersaturation established at zero moment of time. We also

discuss the principle of detailed balance and the curvature effect on the growth rates. Section 1.9 presents the unique cases of i -linear rate constants where the discrete set of rate equations can be integrated exactly. It is shown that the exact solution is given by the time-invariant Polya size distribution, reduced to the Poisson and geometrical distributions in the particular cases. Although irrelevant for the general analysis of nucleation, the obtained solutions are very important for checking the validity of different approximations and for the foregoing analysis of fluctuation-induced broadening of size spectra. In Sect. 1.10, we derive the continuum approximation reducing the infinite set of discrete rate equations to the Fokker-Plank type kinetic equation in partial derivatives for the continuum distribution.

Section 1.11 presents well-known results describing the stationary state in the near-critical region of sizes. It is shown that, at high enough nucleation barrier, the entire size axis can be divided into the subcritical region where the nuclei are at the quasi-equilibrium state, the near-critical region in the stationary state with a size-independent nucleus flux and the super-critical region where the nuclei can grow irreversibly. We take special care to describe in detail the major assumptions and the small parameters justifying the famous Zeldovich expression for the nucleation rate. Although it might seem a little annoying, the nucleation rate and the corresponding stationary distribution are obtained twice based on the discrete and continuum theories to show how and why their results match. We also present the explicit representations for the nucleation rates of 3D and 2D islands in different cases, and discuss the origins of differences in the expressions used previously. It is shown that the stationary distribution reaches the size-independent drift form at the boundary of the near-critical and super-critical regions, if expressed in terms of a certain invariant size. This important feature provides the boundary condition for studying the follow-up growth stages. Section 1.12 starts with a discussion of the mononuclear growth regime in nano-volumes, where the Zeldovich formula for the nucleation rate alone provides sufficient basis for modeling. We then give a preview of consecutive nucleation-condensation stages that are separated in time due to the timescale hierarchy. In brief, the stationary state in the near-critical region of sizes is established almost instantaneously and is then adjusted to the time dependent supersaturation. The nucleation stage under the material influx is short-scale, followed by a much longer stage of regular growth. After that, the nuclei can either coalesce directly or be affected by a special type of indirect interaction leading to the Ostwald ripening, depending on the character of material influx and the island growth law. We discuss the evolution of the mean size of vapor-deposited surface islands at the regular growth stage under the assumption of a narrow size distribution. Finally, we analyze the large time asymptotes of the mean size and supersaturation at different growth indices.

Fig. 1.1 2D lattice gas on a square lattice with the average occupation of $5/36 = 0.14$



1.1 Thermodynamics of Phase Transition

Nucleation theory treats the kinetics of first order phase transitions. The hallmark of such a transition is a discontinuous change of density, the condensation of supersaturated vapor into the liquid droplets in 3D space being a typical example. Aggregation of metastable 2D system of adsorbed atoms (adatoms) into the surface islands is the corresponding analogue in 2D space. Thermodynamics of phase transition provides important information about the equilibrium chemical potential, pressure, and densities of the two phases at a given temperature. Thermodynamic properties of any system undergoing a transition are entirely determined by the equilibrium equation of state. The latter gives a relationship between any three independent thermodynamic parameters, for example: $f(P, V, T) = 0$ or $f(\mu, n, T) = 0$, where P is the pressure, V is the volume, T is the temperature, n is the atomic density (or the concentration), and μ is the chemical potential. A particular form of the equation of state should be obtained from statistical integral with a given Hamiltonian.

One of the most known Hamiltonians which is widely used for the description of different phase transitions in 3D or 2D space is the lattice gas Hamiltonian [1, 2]. In this model, the atoms are placed in the discrete sites $i = 1, 2 \dots N_0$ of 3D or 2D lattice (for example, cubic or rectangular lattice, as shown in Fig. 1.1). The sites are characterized by the occupation numbers $\alpha_i = 0$ or 1 depending on whether the site is empty or occupied. Repulsive interactions are taken into account automatically, since the sites cannot accommodate more than one atom. Attractive interatomic potential $U_{ij} = U(R_{ij}) < 0$ depends on the distance between sites i and j . In the grand canonical ensemble with the fixed chemical potential μ , total number of sites N_0 and temperature T , the configuration part of the statistical sum is given by

$$\Xi(\mu, N_0, T) = \sum_{\alpha_i=0,1} \exp \left(\frac{\mu}{k_B T} \sum_{i=1}^{N_0} \alpha_i - \frac{1}{k_B T} \sum_{(i,j)} U_{ij} \alpha_i \alpha_j \right), \quad (1.1)$$

where k_B is the Boltzmann constant. The summation in the non-diagonal interaction term includes all non-identical atom pairs (i, j) . The statistical averaging accounts for all possible states of N_0 sites with different occupation numbers. The average occupation of sites $\langle \alpha \rangle$ is readily obtained from the statistical sum by

$$\theta \equiv \langle \alpha \rangle = \frac{N}{N_0} = \frac{k_B T}{N_0} \left(\frac{\partial \ln \Xi}{\partial \mu} \right)_T. \quad (1.2)$$

Here, N denotes the total number of atoms or molecules in the system. While the occupation number takes only one of the two discrete values, the average occupation can take any value between zero and one. Obviously, the atomic density is related to θ as $n = n_0 \theta$, where $n_0 = 1/\Omega$ corresponds to the dense lattice packing and Ω is the elementary volume. We will therefore call θ the normalized density, or just density for brevity.

The average volume per one atom in the system with occupation θ equals $1/(n_0 \theta)$. Integrating the known thermodynamic relationship $d\mu = dP/n_0 \theta$ at $T = \text{const}$ along the isotherm, we arrive at

$$P/n_0 = \theta \mu(\theta) - \int_0^\theta d\theta' \mu(\theta'). \quad (1.3)$$

In integration, we use the known asymptotic behaviors of any perfect system without interactions: $\theta \mu(\theta) \rightarrow 0$ and $P(\theta) \rightarrow 0$ at $\theta \rightarrow 0$. This relationship allows one to obtain the equation of state in the form of $P(V, T)$ dependence at the known $\mu(\theta, T)$.

The mean field approximation [1–3] for calculation of the statistical sum given by (1.1) assumes the effective absence, in the temperature range of interest, of local density fluctuations. Applicability of this assumption will be discussed later. With neglect of fluctuations, the local potential field acting upon the atom in a given site i can be approximated by the effective mean field with the average occupation θ :

$$\sum_{(i,j)} U_{ij} \alpha_i \alpha_j \cong \theta \alpha_i \sum_j U_{ij} = -U_0 \theta \alpha_i. \quad (1.4)$$

Here, $U_0 = -\sum_j U_{ij} = -\sum_j U_{0j} > 0$ is the effective energy of attractive interactions, obtained upon the summation of pair potentials over all the interatomic distances. Of course, the potential $U(R_{ij})$ should be sufficiently short-range to enable such a summation. As in the ideal case with no attractive interactions, the insertion of (1.4) into (1.1) leads to the diagonalization of the statistical sum:

$$\Xi = \left[1 + \exp \left(\frac{\mu}{k_B T} + \varphi \theta \right) \right]^{N_0}, \quad (1.5)$$

in which $\varphi = V_0/(k_B T)$ is the dimensionless interaction constant. Using (1.2) and (1.5), we obtain the mean field equation of state that can be put in two equivalent forms

$$\frac{\mu}{k_B T} = -\varphi \theta + \ln \left(\frac{\theta}{1 - \theta} \right); \quad (1.6)$$

$$\frac{\mu}{k_B T_c} \equiv \bar{\mu} = -4\theta + \frac{T}{T_c} \ln \left(\frac{\theta}{1 - \theta} \right). \quad (1.7)$$

Here, by definition, $T_c = (\varphi T)/4 = V_0/(4k_B)$. The second terms in the right hand sides describe the perfect lattice gas with repulsion, while the first terms arise due to the attractive interactions. In dilute systems at $\theta \rightarrow 0$, the chemical potential tends to $\mu = k_B T \ln \theta$, which is the known perfect gas limit.

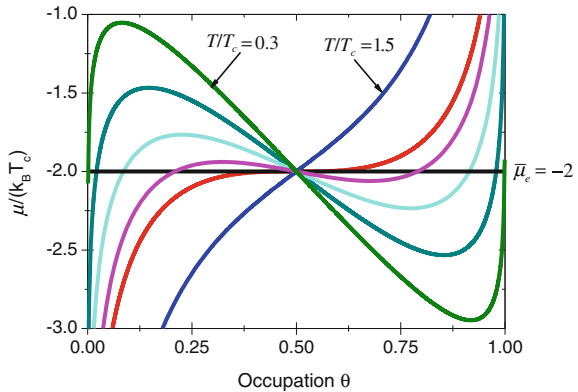
Differentiation of (1.6) with respect to θ at a constant temperature yields: $(\partial\mu/\partial\theta)_T \propto 1 - \varphi\theta + \varphi\theta^2$, showing that the mean field chemical potential monotonously increases when $\varphi < 4$ ($T > T_c$), and reaches its local maximum and minimum at the points

$$\theta_{1s} = \frac{1}{2} \left(1 - \sqrt{1 - \frac{4}{\varphi}} \right); \quad \theta_{2s} = \frac{1}{2} \left(1 + \sqrt{1 - \frac{4}{\varphi}} \right) \quad (1.8)$$

when $\varphi > 4$ ($T < T_c$). The value $\varphi_c = 4$ relates to the inflection of the $\mu(\theta)$ curve at the critical density $\theta_c = 1/2$. Therefore, T_c is the critical temperature. The critical chemical potential is given by: $\mu_c = -V_0/2 = -2k_B T_c$ (yielding $\bar{\mu}_c = -2$) at the inflection point. The two densities defined by (1.8) are the boundaries of the so-called spinodal region. Obviously, they are symmetric relative to the critical occupation of $1/2$.

Graphs of chemical potential given by (1.7) at different temperatures are presented in Fig. 1.2. The wavy regions in the $\mu(\theta)$ dependences below T_c (the so-called van der Waals loops) have no physical sense in equilibrium in view of the known thermodynamic inequality $(\partial\mu/\partial\theta)_T \geq 0$. The loops must therefore be substituted by the horizontal lines relating to the discontinuous change from equilibrium vapor to equilibrium liquid at a constant chemical potential [1–3]. The correct choice of the equilibrium chemical potential cannot be made in an absolute fashion by considering the $\mu(\theta)$ isotherms alone, but requires additional considerations. As is known [1], the two phases with densities θ_{1e} and θ_{2e} at a fixed temperature T are in equilibrium with each other provided that $\mu(\theta_{1e}) = \mu(\theta_{2e})$ and $P(\theta_{1e}) = P(\theta_{2e})$. The equality of chemical potentials implies the absence of diffusion fluxes. The equality of

Fig. 1.2 Normalized chemical potential at different T/T_c decreasing from 1.5 to 0.3. The horizontal line is the equilibrium chemical potential corresponding to the equality of pressures in both phases



pressures yields the compensation of forces acting between the two phases. These two equations enable the unique determination of the phase equilibrium parameters at a given T . Whatever is the form of $\mu(\theta)$, we can write down (1.3) for θ_{1e} and θ_{2e} :

$$p(\theta_{1e}) = \theta_{1e} \bar{\mu}(\theta_{1e}) - \int_0^{\theta_{1e}} d\theta \bar{\mu}(\theta); \quad p(\theta_{2e}) = \theta_{2e} \bar{\mu}(\theta_{2e}) - \int_0^{\theta_{2e}} d\theta \bar{\mu}(\theta), \quad (1.9)$$

where $p \equiv P/(n_0 k_B T_c)$ is the normalized pressure. Subtraction of the first equation from the second one, along with the condition $\bar{\mu}(\theta_{1e}) = \bar{\mu}(\theta_{2e}) \equiv \bar{\mu}_e$, readily gives

$$p(\theta_{2e}) - p(\theta_{1e}) = (\theta_{2e} - \theta_{1e}) \bar{\mu}_e - \int_{\theta_{1e}}^{\theta_{2e}} d\theta \bar{\mu}(\theta). \quad (1.10)$$

From the equality of pressures, the equilibrium chemical potential in both phases thus amounts to the averaged value of $\bar{\mu}(\theta)$ within the interval between θ_{1e} and θ_{2e} :

$$\bar{\mu}_e = \frac{1}{(\theta_{2e} - \theta_{1e})} \int_{\theta_{1e}}^{\theta_{2e}} d\theta \bar{\mu}(\theta). \quad (1.11)$$

Therefore, the equilibrium chemical potential satisfies the Maxwell's rule [1] stating that the areas of the van der Waals loops above and below μ_e must equal each other.

For the specific form of $\mu(\theta)$ given by (1.7), the Maxwell's rule yields

$$\bar{\mu}_e = \bar{\mu}_c = -2, \quad (1.12)$$

the value corresponding to the horizontal line shown in Fig. 1.2. Using this in (1.7), the equilibrium densities are obtained as

$$\theta_{1e} = 1/2 - \Delta\theta_e; \quad \theta_{2e} = 1/2 + \Delta\theta_e, \quad (1.13)$$

where $\Delta\theta_e$ is the solution to the transcendent equation

$$\frac{1}{\Delta\theta_e} \ln \left(\frac{1/2 + \Delta\theta_e}{1/2 - \Delta\theta_e} \right) = \varphi = \frac{4T_c}{T}. \quad (1.14)$$

Obviously, the left hand side contains only the even powers of $\Delta\theta_e$, so that (1.14) has two anti-symmetric solutions at $T < T_c$. We therefore take the value of $\Delta\theta_e > 0$ in (1.13). The resulting equilibrium densities of the dilute and dense phases are symmetric relative to 1/2. The density discontinuity in the transition, also called the equilibrium order parameter, equals $s_e = 2\Delta\theta_e$. The variable $s = 2\Delta\theta = 2\theta - 1$

ranges between -1 and 1 at $0 \leq \theta \leq 1$. The s value can thus be associated with the magnetization (or the averaged spin variable) in the Ising model of magnetism, showing the known analogy between a magnetic system and a lattice gas in grand canonical ensemble [1, 4].

In terms of the spin variable s and the chemical potential counted off its equilibrium value, the above equations of state take the anti-symmetrical form. For example, (1.6) and (1.7) can be re-arranged as

$$h = \frac{\mu - \mu_c}{k_B T} = -\frac{\varphi}{2}s + \ln\left(\frac{1+s}{1-s}\right), \quad \bar{\mu} - \bar{\mu}_c = -2s + \frac{T}{T_c} \ln\left(\frac{1+s}{1-s}\right), \quad (1.15)$$

or in a more conventional inverted form

$$s = \tanh\left(\frac{h}{2} + \frac{T_c}{T}s\right). \quad (1.16)$$

Here, h stands for the appropriately normalized external magnetic field. Graphical representation of phase transition at $h = 0$ is shown in Fig. 1.3, where the functions s and $\tanh[(T_c/T)s]$ are plotted against the magnetization s . The curves meet only at the trivial point $s_e = 0$ above T_c , corresponding to a stable disordered state. At $T < T_c$, (1.16) has two stable anti-symmetric solutions $\pm s_e$ describing two anti-symmetric ordered states with non-zero magnetization that rapidly approach ± 1 as the temperature decreases.

Let us now see how the mean field equation of state looks like in terms of the more usual pressure-volume isotherms. Inserting (1.7) into (1.3) and integrating, we arrive at

$$\frac{P}{n_0 k_B T_c} \equiv p = -2\theta^2 - \frac{T}{T_c} \ln(1 - \theta). \quad (1.17)$$

Fig. 1.3 Illustration of magnetic phase transition at zero external field

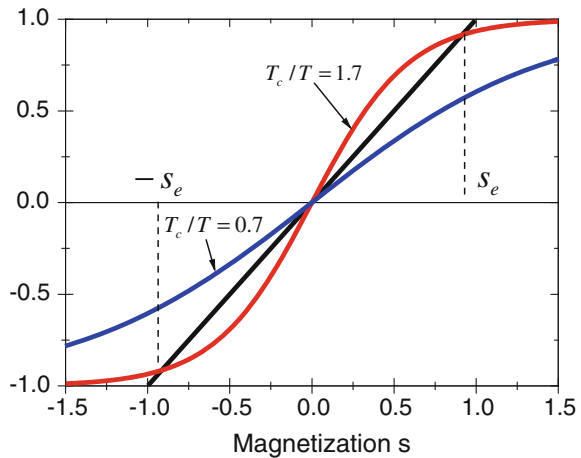
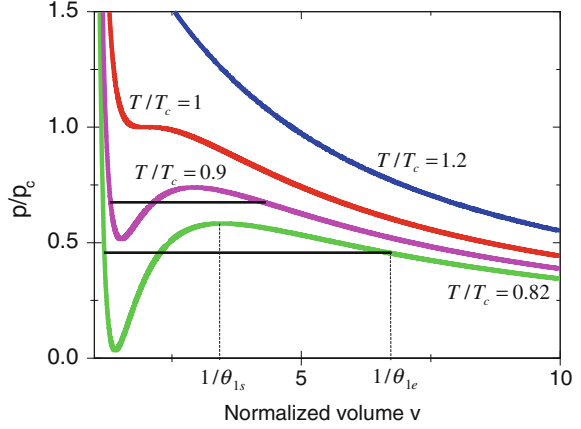


Fig. 1.4 Pressure-volume diagrams at different T/T_c . The horizontal lines correspond to the Maxwell's rule. The values of θ_{le} and θ_{ls} are the equilibrium occupation and the spinodal boundary, respectively



This equation gives correctly the perfect gas limit $P = nk_B T$ at $\theta \rightarrow 0$ and yields an infinite pressure at $\theta \rightarrow 1$. The critical pressure at $T = T_c$ and $\theta_c = 1/2$ is readily obtained as $p_c = \ln 2 - 1/2$. Introducing the normalized volume $v = V/\Omega = 1/\theta$, (1.17) can be put in the form [3]

$$\frac{p}{p_c} = -\frac{2b_0}{v^2} - \frac{b_0 T}{T_c} \ln \left(1 - \frac{1}{v} \right) \quad (1.18)$$

with $b_0 = 1/(\ln 2 - 1/2) \cong 5.177$. The pressure-volume isotherms obtained from (1.18) at different T/T_c are shown in Fig. 1.4. The curve at the critical temperature has the inflection point at $\theta_c = 1/2$ (corresponding to $v_c = 2$) and $p = p_c$. The spinodal points are obtained by putting the derivative of (1.15) to zero and are the same as given by (1.8). The horizontal lines in Fig. 1.2 at $T < T_c$ correspond to the Maxwell's rule and yield the same equilibrium densities as those given by (1.13) and (1.14). Finally, we underline universality of these equations of state. Indeed, as follows from (1.7) and (1.18), all systems having the same T/T_c would obey exactly identical thermodynamic laws in terms of the appropriately normalized variables.

As mentioned above, neglect of local fluctuations of the order parameter, which is the core assumption in any mean field theory (the van der Waals gas, the Weiss theory of magnetism [1], the Landau theory of phase transitions and its spatially inhomogeneous generalization [4]), is not always valid. Thermodynamic fluctuations are known to increase drastically as temperature approaches T_c , so that the correlation radius tends to infinity at $T \rightarrow T_c$. This gives rise to a special type of fluctuational behavior, called the critical behavior, where the fluctuation-induced interactions become more important than those defined by the deterministic interaction potential [4]. As a consequence, thermodynamic properties near T_c only weakly depend on the details of interatomic potential. Rather, they are affected by the type of symmetry in the system, the number of components of the order parameter, the

Table 1.1 Scaling exponents for gas–liquid transitions in 3D space

Physical value	Order parameter, s_e	Compressibility, K_T	Heat capacity, C_P	Pressure, $\Delta P = P_c - P$	Correlation radius, r_c	Correlation function, $G(r)$
Notation of exponent	β	γ	α	δ	ν	η
Definition	$s_e \propto \tau^\beta$	$K_T \propto \tau^{-\gamma}$	$C_P \propto \tau^{-\alpha}$	$\Delta P \propto s_e^\delta$	$r_c \propto \tau ^{-\nu}$	$G \propto r^{-d+2-\eta}$
Experiment	0.34 ± 0.01	1.22 ± 0.02	0.12 ± 0.04	4.6 ± 0.2	0.63 ± 0.01	0.05 ± 0.01
Mean field values	0.5	1	0	3	0.5	0
ε -expansion	0.34	1.244	0.077	4.46	0.626	0.037

cutoff radius of interactions (short-range or long-range forces) and, very importantly, by the space dimension. Such a behavior naturally leads to the universality, where the asymptotic power law dependences of different thermodynamic values at $T \rightarrow T_c$ are well described by the critical exponents that are independent of interaction potential.

For a spatially homogeneous system, the four critical exponents are introduced by definitions summarized in Table 1.1. In terms of gas–liquid transition, they reveal the leading power law dependences of the density discontinuity $s_e = 2\Delta\theta_e$, isothermal compressibility $K_T = \theta^{-1}(\partial\theta/\partial P)_T$, heat capacity at a constant pressure $C_P = T(\partial S/\partial T)_P = -T(\partial^2\mu/\partial T^2)_P$ on $\tau = (T_c - T)/T_c$, and pressure-density dependence $P(s_e)$ along the critical isotherm. The other two exponents describe the properties of density–density correlation function [4] and will be discussed in the next paragraph.

Table 1.1 summarizes the known experimental values of the critical exponents for 3D vapor–liquid transitions according to the data of [4]. Let us now consider the critical behavior in the mean field theory. First, the Taylor expansion of (1.16) in s at $T \rightarrow T_c$ leads to

$$\bar{\mu}(s) - \bar{\mu}_c \cong -2\tau s + \frac{2s^3}{3}. \quad (1.19)$$

Putting the left hand side to zero at $\tau > 0$, we obtain $s_e = (3\tau)^{1/2}$ at $T < T_c$, yielding $\beta = 1/2$. Above T_c , the only possible solution is $s_e = 0$. Similar expansion of p defined by (1.17) gives

$$p(s) - p_c \cong -\tau s - \frac{\tau s^2}{2} + \frac{s^3}{3}. \quad (1.20)$$

At $\tau = 0$ relating to the critical isotherm, this is reduced to $p - p_c \propto s^3$, corresponding to $\delta = 3$. The leading linear term in the right hand side shows that $K_T \propto \tau^{-1}$, yielding $\gamma = 1$. Further, from (1.19) and (1.20) it follows that

$$\bar{\mu} - \bar{\mu}_c \cong 2(p - p_c) + \tau s^2. \quad (1.21)$$

At $\tau < 0$ where $s_e = 0$, the heat capacity $C_P = 0$. At $\tau > 0$, $s_e^2 = 3\tau$, resulting in $-T_c(\partial^2\bar{\mu}/\partial T^2)_p = 6/T_c$. Returning to the dimensional chemical potential $\mu = k_B T_c \bar{\mu}$, we get the value of $C_P = 6k_B$ below T_c , reflecting a discontinuous change of the heat capacity while passing the critical temperature. Such a discontinuity relates, however, to $\alpha = 0$ by its definition given in Table 1.1. It is noteworthy that the mean field exponents do not depend on the space dimension, in contrast to their experimental values and those obtained by computer simulations.

The mean field exponents summarized in Table 1.1 are obviously far beyond the error bars in experimental data. As expected, neglect of fluctuations is incorrect near the critical point, leading to the wrong values of critical exponents. This discrepancy has led to an impressive development of a principally new approach in studies of critical phenomena based on the scaling hypothesis for the fluctuational field of the order parameter [5, 6]. The turning point in these studies has been the so-called ε -expansion for the critical indices that demonstrates a surprisingly good quantitative correlation with the experiment (see Table 1.1). Summarizing, the mean field theory fails to quantify the near-critical behavior, although predicting correctly all thermodynamic values in the critical point itself [1], as well as giving a reasonable qualitative description of phase separation process in general.

In practice, nucleation theory always deals with systems at low enough temperatures, where the fluctuations are weak and the mean field thermodynamics is exactly applicable. Indeed, the very notion of a “nucleus” can only be used if the entire system can be subdivided into dilute and dense phases separated by a distinct boundary, a liquid droplet surrounded by an almost perfect vapor being the typical case. Such a separation requires a large density discontinuity between the equilibrium phases, which occurs only at temperatures well below T_c . However, non-classical kinetic scenarios of phase transition can be observed even at low T in certain cases. The most common scenarios are discussed in the next section.

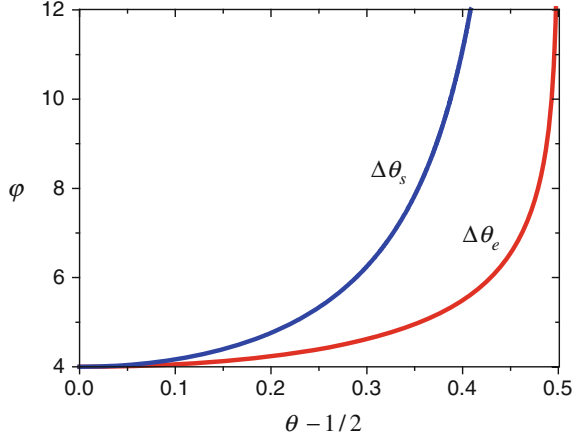
1.2 Scenarios of Phase Transition

As is seen from Figs. 1.2 and 1.4, as temperature decreases, the equilibrium densities θ_{1e} and θ_{2e} rapidly approach zero and one, respectively. The boundaries of spinodal region also do so, but their relaxation is slower. This feature is illustrated in Fig. 1.5, where the $\Delta\theta_e$ and the halfwidth of the spinodal region $\Delta\theta_s = \sqrt{1 - 4/\varphi}/2$ are plotted against the interaction constant $\varphi = 4T_c/T$. At low enough temperatures, $T < 0.5T_c$ (corresponding to $\varphi > 8$), the two solutions to (1.14) simplify to the following expressions

$$\theta_{1e} = \exp\left(-\frac{2T_c}{T}\right); \quad \theta_{2e} = 1 - \exp\left(-\frac{2T_c}{T}\right). \quad (1.22)$$

In this low-temperature domain, the occupation of the dilute phase is smaller than 0.02, while the condensed phase is denser than 0.98. The first of (1.22) is the analogue

Fig. 1.5 Halfwidth of spinodal region and density discontinuity versus φ



of the Clapeyron-Clausius equation for the equilibrium density in vapor. The quantity $2k_B T_c$ is called the hidden condensation heat.

In thermodynamics, the van der Waals loops on the $\mu(\theta)$ isotherms at $T < T_c$ are substituted by the horizontal lines corresponding to the phase equilibrium. However, the loops are useful in the kinetic theory of phase transitions [3], as demonstrated in Fig. 1.6. Considering a condensation type of transition, the region between θ_{1e} and θ_{1s} relates to the metastable states where the vapor chemical potential is larger than the equilibrium. The driving force for an isothermal phase transition from a metastable state to a liquid (which is at the equilibrium chemical potential) is determined by

$$\Delta\mu = \mu(\theta) - \mu_e. \quad (1.23)$$

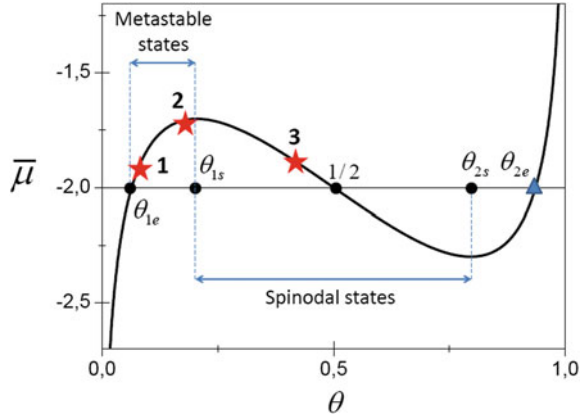
In a dilute metastable system, the driving force writes down as $\Delta\mu = k_B T \ln(\zeta + 1)$, where

$$\zeta = n_1/n_{1e} - 1 \quad (1.24)$$

is the supersaturation, n_1 is the concentration in a metastable phase and $n_{1e} = \theta_{1e}/\Omega$ is its equilibrium concentration. The maximum possible supersaturation at a given temperature is determined by $\zeta_{\max} = \theta_{1s}/\theta_{1e} - 1$. The spinodal region between θ_{1s} and θ_{2s} corresponds to unstable states with a negative derivative of chemical potential with respect to density.

Let us now consider possible scenarios of phase transition, schematized in Fig. 1.6. In order to better illuminate our qualitative analysis, we adopt the following model for the free energy (measured in the units of $k_B T$) of forming a 3D nucleus consisting of i monomers (atoms, molecules, adatoms etc.): $F(i) = ai^{2/3} - \ln(\zeta + 1)i$. The first term stands for the surface energy of 2D interphase boundary, whose area scales as $i^{2/3}$. It is always positive because the formation of nucleus surface is energetically unfavorable. The second term gives the change in the volume energy of

Fig. 1.6 1 low supersaturation, classical nucleation theory; 2 high supersaturation, field theory of scalar order parameter; 3 spinodal decomposition via increasing density oscillations



i monomers transferred from a metastable vapor into a liquid. This term is negative at $\zeta > 0$. Therefore, condensation process is kinetically suppressed due to an energetically unfavorable process of building the nucleus surface. A more detailed analysis of different types of the formation energies will be given later on. Since the two terms scale differently with i , the formation energy reaches its maximum $F \equiv F(i_c) = (4a^3)/[27 \ln^2(\zeta + 1)]$ at the critical number of monomers $i_c = (8a^3)/[27 \ln^3(\zeta + 1)]$. The maximum value of the formation energy F is called the activation energy for nucleation, or the nucleation barrier. This barrier should be surpassed to form an irreversibly growing nucleus. The particle consisting of i_c monomers is called the critical nucleus, which is in unstable equilibrium with a supersaturated environment. The nucleation barrier and the critical number of monomers tend to infinity at $\zeta \rightarrow 0$ (no transition) and to zero at $\zeta \rightarrow \infty$ (neither barrier to surpass nor unstable critical nucleus). As shown in Fig. 1.6, a metastable vapor can in principle be “prepared” in any state between θ_{1e} and θ_{2s} . When the initial supersaturation is low enough to ensure that the critical size i_c and the nucleation barrier F are much larger than one, and the density discontinuity $2\Delta\theta$ is close to one, the classical nucleation theory [3, 7–30] is directly applicable. Its major assumptions, such as macroscopic nuclei, the distinct boundaries that can be characterized by their surface energies, and the smallness of thermodynamic fluctuations in the subcritical region below i_c , can be well justified. This case, corresponding to point 1 in Fig. 1.6, is studied throughout this book.

Increasing the initial concentration of vapor toward θ_{1s} (point 2 in Fig. 1.6) and ultimately entering the spinodal region (point 3 in Fig. 1.6) leads to a rather different behavior [3]. First, the correlation radius can get larger than the characteristic size of nuclei. Second, thermodynamic fluctuations perturb the subcritical region so that the size distribution there cannot remain quasi-equilibrium. Third, internal structure of nuclei might be so sophisticated that the usual notions of the interfacial boundary and surface energy would no longer apply. Whenever the initial spatially homogeneous state falls within the spinodal region (for example, at $\theta_0 = 1/2$), the system is

thermodynamically unstable from the beginning. In view of $d\mu/d\theta < 0$, the diffusion flux in the spinodal region is directed against rather than along the density gradient, leading to the so-called “uphill” diffusion [31]. When the diffusion goes uphill, the amplitude of fluctuation-induced density oscillations will increase with time. Such system cannot be described in terms of size and number of nuclei, at least at the beginning of phase separation. The phase transition scenario via the increasing density oscillations is usually called the spinodal decomposition [32].

Theoretical analysis of highly metastable systems requires quite different approaches from those used in the case of low supersaturations. One of the non-classical approaches treats the phase transition as the relaxation of spatially inhomogeneous scalar field of the order parameter $s(\vec{r}, t) = 2\Delta\theta(\vec{r}, t)$, where \vec{r} is the spatial coordinate and t is time [3, 33–35]. The general form of the field equation can be written down as

$$t_* \frac{\partial s}{\partial t} = -\frac{\delta F}{\delta s} + f_*. \quad (1.25)$$

Here, t_* is the kinetic coefficient, $F[s]$ is the free energy functional [4] in the units of $k_B T$ per site, and f_* is the external field. The change of spatially inhomogeneous part of F at the fixed T and the total number of sites N_0 writes: $dF = h(s)ds$, where $h(s)$ is defined in (1.15). Therefore, the free energy functional can be presented in the form

$$F[s] = \int d\vec{r} \left[\frac{R_s^2}{2} (\nabla s)^2 + E(s) \right]; E(s) = \int ds h(s), \quad (1.26)$$

in which R_s is the scale factor determined by the cutoff radius of interaction potential. The first contribution under the integral of (1.26) describes the leading term of the series expansion of the field Hamiltonian in ∇s according to the Ginsburg-Landau theory [4]. Taking the functional derivative of (1.26), (1.25) is reduced to

$$t_* \frac{\partial s}{\partial t} = R_s^2 \Delta s - h(s) + f_*. \quad (1.27)$$

Realistically, (1.27) makes sense only for small enough $s_1 = s - s_0$, where s_0 is the initial spatially homogeneous state. We first consider the case where point 2 in Fig. 1.5 corresponds to the left boundary of the spinodal region: $s_0 = -\sqrt{1-4/\varphi}$. The function h here can be presented as $h(s_1) \cong a - bs_1^2$ with positive constants a and b . Upon appropriate rescaling, (1.27) can be put as

$$\frac{\partial s_1}{\partial t} = \Delta s_1 + 2(s_1^2 - 1) + f_*. \quad (1.28)$$

This equation describes the behavior of highly metastable systems near the spinodal boundary. As shown in [36] in the case of 2D adatom systems, (1.28) is capable of describing the stationary configuration corresponding to the critical nucleus, the relaxation of the order parameter in the linear approximation, and, most importantly, the nucleation rate which is given by $I(\zeta) = I(\zeta_{\max}) \exp[-\text{const}(\zeta_{\max} - \zeta)^2]$.

When point 3 in Fig. 1.6 is fixed at $\theta_0 = 1/2$ and the temperature is close to T_c , the behavior of $h(s)$ is given by the right hand side of (1.19). Using this in (1.27) and rescaling, the equation for the order parameter takes the form

$$\frac{\partial s}{\partial t} = \Delta s + s(s_e^2 - s^2) + f_*. \quad (1.29)$$

Here, s_e corresponds to the equilibrium spatially homogeneous states. As expected, (1.29) has periodic solutions already in the linear approximation in u . Separation of the initially space-uniform state at $s_0 = 0$ into the phases with $s_e = \pm\sqrt{3\tau}$ evolves via the increasing density fluctuations, starting from linear but then acquiring an essentially non-linear character. More details on the kinetics of spinodal decomposition in the systems described by (1.29) can be found, for example, in [37].

Stationary (1.29) in the linear approximation above T_c takes the form

$$-\Delta s + s/r_c^2 = f_*, \quad (1.30)$$

where $r_c = 1/\sqrt{3|\tau|}$. The Green function of this equation in 3D space, corresponding to the point source $f_*(r) = \delta(r)$ in the origin, is given by

$$G(r) = \frac{\exp(-r/r_c)}{4\pi r}. \quad (1.31)$$

Clearly, the r_c parameter plays a role of the correlation radius. The obtained Green function is closely related to the correlation function of the order parameter $\langle s(\vec{r})s(0) \rangle$. As discussed above, r_c discontinuously increases near T_c . The mean field theory thus predicts the critical exponent $\nu = 1/2$ for its temperature behavior. At $r \ll r_c$, $G(r)$ scales as r^{-1} , yielding $\eta = 0$. This completes the set of mean field critical exponents given in Table 1.1. We note that the correlation function given by (1.31) is of the Ornstein–Zernike type, as in the standard Landau theory of phase transitions [4]. This is not surprising, since the Taylor expansion of chemical potential near the critical point reduces the lattice gas model to the Landau-type Hamiltonian.

1.3 Laplacian Pressure and Gibbs–Thomson Effect

Thermodynamic parameters of nanoparticles such as pressure and chemical potential are essentially size-dependent. One of the most important manifestations of size-dependent effects is a tremendous increase of the equilibrium pressure inside a nanoparticle, and the corresponding elevation of its chemical potential. Both effects are driven by the surface curvature [38]. Let us briefly discuss how the surface energy is introduced in thermodynamics. Whenever the system consists of two or more phases, for example, liquid droplets or solid particles surrounded by vapor,

all thermodynamic potentials are modified by the surface energy term $\sum_k \gamma_k S_k$. The index k accounts for different surfaces of the area S_k having different surface energies γ_k (J/m²). Typical values of γ in liquids and solids are of the order of 1 J/m². The surface energy must be positive, because the minimum of thermodynamic potential is reached with the minimum surface area at a given volume. Otherwise, the two phases could not be separated at all. In the case of a solid–solid heterogeneous interface, the corresponding γ is usually called the interface energy. The microscopic origin of the surface energy is the dangling bonds created, for example, by the dissection of crystal with a certain crystallographic plane. Some dangling bonds can be passivated by the species adsorbed from vapor environment. That is why the surface energy generally depends on the chemical composition of both phases. The interface energy originates from microscopic interactions between dissimilar atoms at the interface. In isotropic liquids, the surface energy does not vary along the surface, while the surface energy of crystal solids depends on the crystallographic orientation of the corresponding planes terminating the particle.

We now consider a particular case of liquid or solid particle (phase 2) of surface area S surrounded by vapor (phase 1). At a constant temperature in both phases and under the constrain of the fixed volume $V = V_1 + V_2$, the particle of a given size is in equilibrium with vapor when the grand potential of the entire system

$$\Psi = -P_1 V_1 - P_2 V_2 + \gamma S \quad (1.32)$$

reaches the extremum. It is noteworthy that this extremum relates not to the minimum, but to the maximum of Ψ , showing that the equilibrium state is unstable. Taking the differential of Ψ at $V = \text{const}$,

$$d\Psi = (P_1 - P_2)dV_2 + \gamma dS, \quad (1.33)$$

and putting it to zero, the pressure difference is obtained in the form

$$P_2 - P_1 = \gamma \frac{dS}{dV_2}. \quad (1.34)$$

Obviously, the dS/dV_2 scales inversely proportional to the linear size of particle R , yielding the equality of pressures in the bulk limit $R \rightarrow \infty$. Otherwise, P_2 is larger than P_1 , with the difference rapidly increasing as the particle size shrinks. The additional pressure in the condensed phase $\Delta P = P_2 - P_1$ given by (1.34) is called the Laplacian pressure.

We now show how the Laplace formula allows one to find the pressures in the two phases separately, as well as the chemical potential corresponding to the unstable equilibrium. We write down the conditions of equilibrium between the vapor and condensed phases with finite and infinite R as

$$\mu_1(P_1) = \mu_2(P_2) \quad (1.35)$$

and

$$\mu_{1\infty}(P_e) = \mu_{2\infty}(P_e) = \mu_e. \quad (1.36)$$

Here, ∞ denotes the $R \rightarrow \infty$ limit, where the two phases are at the same equilibrium pressure P_e and chemical potential μ_e . Subtracting the second equation from the first one, we note that the vapor chemical potential depends on its pressure as $k_B T \ln P_1$, yielding $\mu_1(P_1) - \mu_1(P_e) = k_B T \ln(P_1/P_e)$. The chemical potential in the condensed phase at a constant temperature is given by $d\mu_2 = \Omega dP_2$, where Ω is the elementary volume. Assuming that the particle is incompressible, we get: $\mu_2(P_2) - \mu_2(P_e) = \Omega(P_2 - P_e)$. For a small enough particle, P_2 should be much larger than P_e . This allows us to write approximately $P_2 - P_e \cong P_2 - P_1$ and to use (1.34) for $P_2 - P_e$. In this approximation, the Gibbs–Thomson modification of the equilibrium chemical potential in both phases is obtained in the form

$$\mu_1(P_1) = \mu_2(P_2) = \mu_e + \Omega\gamma \frac{dS}{dV_2}. \quad (1.37)$$

As for the vapor pressure, it increases exponentially with decreasing the particle size due to a high compressibility of vapor:

$$P_1 = P_e \exp\left(\frac{\Omega\gamma}{k_B T} \frac{dS}{dV_2}\right). \quad (1.38)$$

The derivative dS/dV_2 , entering the expressions for the Laplacian pressure and the Gibbs–Thomson effect on the chemical potential, depends strongly on the system geometry. Some typical geometries are shown in Fig. 1.7. In the case of a spherical liquid droplet of the radius R surrounded by vapor, $S = 4\pi R^2$ and $V_2 = (4\pi/3)R^3$, yielding $dS/dV_2 = 2/R$. If the “particle” is a solid cylinder of the radius R and length L , its sidewall surface area and volume are $S = 2\pi RL$ and $V_2 = \pi R^2 L$, respectively. If this cylinder can extend only radially ($L = \text{const}$), we get $dS/dV_2 = 1/R$. When a liquid droplet is seated on top of a cylindrical solid rod of the radius R , it has the shape of a spherical cap with the contact angle β . The surface area and the volume of a spherical cap are given by

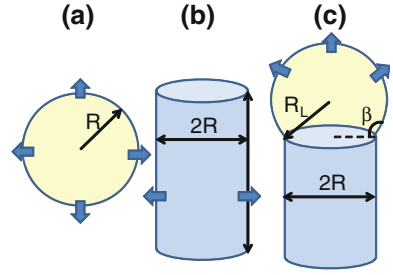
$$S = \frac{2\pi R^2}{1 + \cos \beta} \quad (1.39)$$

and

$$V_2 = \frac{\pi R^3}{3} f(\beta); \quad f(\beta) = \frac{(1 - \cos \beta)(2 + \cos \beta)}{(1 + \cos \beta) \sin \beta}. \quad (1.40)$$

At $R = \text{const}$, the droplet size can change only by varying the contact angle β . In view of $df(\beta)/d\beta = 3/(1 + \cos \beta)^2$, we obtain $dS/dV_2 = (2 \sin \beta)/R = 2/R_L$, where R_L is the droplet radius (see Fig. 1.7c). In all the cases considered, the size-dependent terms are inversely proportional to the radius of the surface curvature.

Fig. 1.7 Model geometries of particles surrounded by vapor, the arrows show the moving surfaces



Using the obtained relationships in (1.37), the Laplacian pressure ΔP and the corresponding Gibbs–Thomson modification of chemical potential $\Delta\mu = \mu - \mu_e$ are given by

$$\text{Spherical droplet of the radius } R : \Delta P = \frac{2\gamma}{R}; \Delta\mu = \frac{2\Omega\gamma}{R}; \quad (1.41)$$

$$\text{Cylinder of the radius } R : \Delta P = \frac{\gamma}{R}; \Delta\mu = \frac{\Omega\gamma}{R}; \quad (1.42)$$

$$\text{Spherical cap on a cylinder of the radius } R : \Delta P = \frac{2\gamma \sin \beta}{R}; \Delta\mu = \frac{2\Omega\gamma \sin \beta}{R}. \quad (1.43)$$

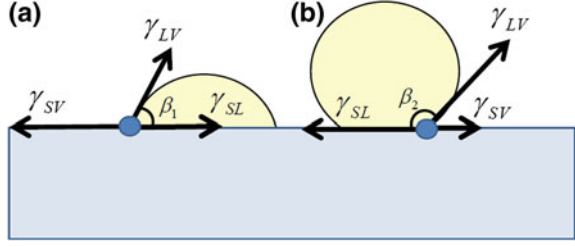
To give a numerical estimate of the curvature effect, consider a 10 nm radius GaAs nanowire growing from a liquid Au-Ga droplet (with neglect of As due to its low solubility in Au), at $\beta \cong \pi/2$. The droplet surface energy in this case must be between that of pure liquid Ga and Au (0.72 and 1.14 J/m², respectively [39]), yielding a huge Laplacian pressure between 0.14 and 0.23 GPa. As discussed later on, this has a major impact of nanowire growth: at a given vapor pressure, smaller droplets will desorb more atoms than larger ones, which will suppress the nanowire growth from droplets smaller than a certain critical radius.

1.4 Contact Angle

Consider a liquid droplet seated on a planar solid surface and surrounded by vapor, as illustrated in Fig. 1.8. The surface energies of such a three-phase system are denoted as γ_{LV} , γ_{SV} and γ_{SL} at the liquid–vapor, solid–vapor and solid–liquid phase boundaries, respectively. The surface energy of the system writes down as

$$G = \gamma_{LV} \frac{2\pi R^2}{1 + \cos \beta} + \gamma_{SL} \pi R^2 + \gamma_{SV} (S_0 - \pi R^2), \quad (1.44)$$

Fig. 1.8 Liquid droplet on solid surface with equilibrium contact angle $\beta_1 < \pi/2$ (a) and $\beta_2 > \pi/2$ (b). The dot denotes the triple phase line



where β is the contact angle, R is the radius of the base and $S_0 = \text{const}$ is the surface area of the solid. We aim at finding the equilibrium contact angle relating to the minimum of surface energy at the fixed droplet volume V given by (1.40).

The surface energy G is generally a function of two variables, R and β , which are related to each other by the condition $V = \text{const}$. Writing the volume differential in the form

$$dV = \pi R^2 \left[f(\beta) dR + \frac{R}{3} \frac{df(\beta)}{d\beta} d\beta \right],$$

we derive:

$$R d\beta = -(2 + \cos \beta) \sin \beta dR. \quad (1.45)$$

After simple calculations, the differential dG amounts to

$$dG|_{V=\text{const}} = (\gamma_{SL} - \gamma_{SV} + \gamma_{LV} \cos \beta) 2\pi R dR. \quad (1.46)$$

Therefore, the system is in equilibrium when the contact angle satisfies the Young's equation [38]:

$$\gamma_{SV} = \gamma_{SL} + \gamma_{LV} \cos \beta_*. \quad (1.47)$$

From (1.46), it can be easily seen that the second differential of G is always positive at $\beta = \beta_*$. The Young's contact angle therefore corresponds to the minimum surface energy. The mechanical interpretation of the Young's equation is quite obvious: it requires the compensation of horizontal surface forces acting upon the triple phase line, as shown in Fig. 1.8. At the same time, the compensation of vertical surface force directed upward should lead to a certain reconstruction of the solid structure under the droplet.

With arbitrary surface energies, (1.47) can be satisfied with a positive contact angle only if $\gamma_{SV} < \gamma_{SL} + \gamma_{LV}$. In this case, the droplet does not wet the solid surface. The case of $\gamma_{SV} > \gamma_{SL}$ yields $\beta_* < \pi/2$. The condition $\gamma_{SV} < \gamma_{SL}$ corresponds to $\beta_* > \pi/2$, with the extreme case of $\beta_* = \pi$ being reached at $\gamma_{SV} = \gamma_{SL} - \gamma_{LV}$. From these considerations, the three surface energies must satisfy the inequality $\gamma_{SV} \leq \gamma_{SL} - \gamma_{LV}$, which is not at all guaranteed in the general case. However, the solid-vapor surface energy could be modified by monolayer adsorption, and such an adsorption will necessarily take place if the last inequality is not met without it [38].

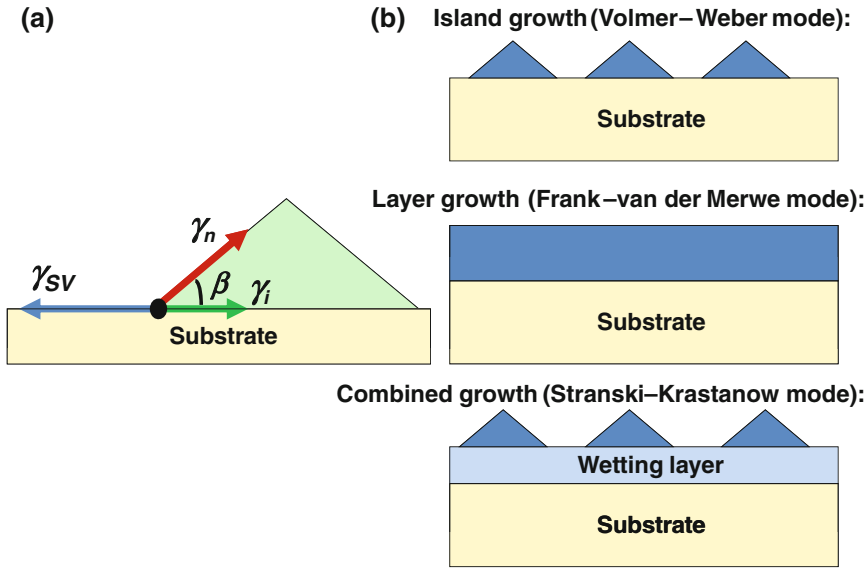


Fig. 1.9 Surface energetics of the crystal island (a) and the surface growth modes (b)

When $\gamma_{sv} > \gamma_{sl} + \gamma_{lv}$, the Young's equation cannot be satisfied, and the liquid wets the solid surface. The wetting occurs, for example, when the solid–vapor surface is much more energetic than the liquid–vapor one. Formation of a 2D liquid film is then energetically preferred to the liquid agglomeration into 3D droplets where some part of the solid surface remains exposed to vapor.

The Young's equation is sometimes applied to the case of solid surface islands, for example, in the elementary classification of the growth modes of thin solid films [40–42], as shown in Fig. 1.9a. Surface film can either grow layer-by-layer in the Frank–van der Merwe mode, or form 3D islands on a bare surface (the Volmer–Weber mode). In some specific cases, the combined Stranski–Krastanow growth is observed, where the film forms the so-called 2D wetting layer at the beginning, but then the growth is transformed into a 3D island mode. These modes are schematized in Fig. 1.9b. The Young's equation can now be re-written in the form

$$\gamma_{sv} = \gamma_i + \gamma_n \cos \beta. \quad (1.48)$$

Here, γ_i is the interface energy at the planar solid–solid boundary under the island and γ_n is the surface energy of the island facet plane (Fig. 1.9a). The facets should relate to the lowest among the local minima of the crystal surface energy, while the global minimum is usually reached in the in-plane direction. In the case of homoepitaxy, $\gamma_i = 0$ and $\gamma_n = \gamma_{sv}$ for the substrate plane, showing that homoepitaxial layers should be stable against faceting and grow in 2D form (however, nucleation of upper layers before the completion of the lower ones is not always guaranteed). The Volmer–Weber islands form during heteroepitaxy if $\gamma_{sv} < \gamma_i + \gamma_n$, when the

deposit-substrate interface is highly energetic, and the surface energy of the deposit is also sufficiently large compared to the substrate. Heteroepitaxial layer will grow in 2D form in the opposite case $\gamma_{SV} > \gamma_i + \gamma_n$, where the substrate is more energetic than the “sandwich” composed of the deposit-vapor surface and the deposit–substrate interface.

The Stranski-Krastanow growth on a dissimilar surface cannot be fully explained on purely surface energetic grounds. Indeed, while 2D growth of the first few monolayers can be energetically preferred, it is difficult to see why 3D islands prefer to form on the similar substrate, which is effectively the homoepitaxy case. One can thus suggest that 3D islands gain some decrease in the volume energy compared to 2D thin film. This is exactly what happens in lattice mismatched material systems, where the driving force for 2D-3D growth transformation is the relaxation of elastic stress (induced by the lattice mismatch) on free side facets. Very importantly, sufficiently small 3D islands remain dislocation-free. The Stranski-Krastanow growth of coherent strained islands will be studied in detail in Chap. 3.

We now consider the freestanding “nanowire” geometry with the liquid droplet seated on the nanowire top. The standard system configuration, where the droplet wets the top facet but not the sidewalls (the non-wetting case) [43, 44] is shown schematically in Fig. 1.10a. We assume the wire as being a straight cylinder of a constant radius and the droplet in the form of a spherical cap with the contact angle $\beta_0 > \pi/2$. The choice of β_0 will be discussed later on. We consider five surface energies shown in Fig. 1.10a–c: those of the horizontal solid–liquid surface γ_{SL} , the liquid–vapor surface γ_{LV} , the top facet in contact with the vapor γ_{SV} , the nanowire sidewalls in contact with the vapor γ_{WV} , and the vertical solid–liquid surface γ_{SL}^l . Let us first study the stability of the triple phase line position at the outer periphery of the nanowire top. When the triple phase line is shifted horizontally toward the wire center (Fig. 1.10b), the back surface force $F_h = \gamma_{SV} - \gamma_{LV} \cos \beta_0 - \gamma_{SL}$ is positive in view of $\gamma_{SV} > \gamma_{SL}$ (this inequality should pertain in most cases) and thus returns the triple phase line to its original position. When the triple phase line is randomly shifted downward (Fig. 1.10c), the vertical force $F_0 = \gamma_{LV} \sin \beta_0 + \gamma_{SL}^l - \gamma_{WV}$ is directed upward provided that

$$\gamma_{WV} < \gamma_{LV} \sin \beta_0 + \gamma_{SL}^l. \quad (1.49)$$

This inequality, obtained here as the condition for stability of the triple phase line at the top periphery, is exactly identical to the Nibol’sin-Shchetinin [43] and Glas [45] conditions that are very important in studying the so-called vapor–liquid–solid growth of nanowires [46, 47]. This will be discussed further in Chap. 4.

Let us now see what happens if the inequality (1.49) is not satisfied, that is, when

$$\gamma_{WV} > \gamma_{LV} \sin \beta_0 + \gamma_{SL}^l. \quad (1.50)$$

Opposite to the previous case, whenever the triple phase line moves slightly downward, the surface force is also directed downward and tends to increase the part of nanowire height y wetted by the liquid (the wetting case), as shown in Fig. 1.11a.

Under the constraint of a fixed liquid volume V and radius R , the penetration of wire cylinder into the droplet leads to the increase of contact angle β . As β increases, the vertical force $F = \gamma_{wv} - \gamma_{lv} \sin \beta - \gamma_{sl}^l > 0$ can only increase. Therefore, any configuration with y between zero and $y_{\max} = -2R \cot \alpha \beta_{\max}$ is unstable, and the droplet will continue sliding down until the cylinder hits the droplet surface (Fig. 1.11b).

Configuration shown in Fig. 1.11b relates to the minimum surface energy with a spherical droplet under the condition given by (1.50). This is the consequence of the following theorem [48]:

The surface energy of the system incorporating the droplet and the wire of length $L = \text{const}$,

$$G = \frac{2\pi R^2}{1 + \cos \beta} \gamma_{LV} + \pi R^2 \gamma_{SL} + 2\pi R y \gamma_{SL}^l + 2\pi R(L - y) \gamma_{wv}, \quad (1.51)$$

under the condition of a fixed liquid volume

$$V = \frac{\pi R^3}{3} \frac{(1 - \cos \beta)^2 (2 + \cos \beta)}{\sin^3 \beta} - \pi R^2 y = \text{const} \quad (1.52)$$

and at a constant R , has the minimum either at $\beta = \beta_0$ (relating to $y = 0$) or at $\beta = \beta_{\max}$ (relating to $y = y_{\max}$) when the inequality (1.49) is satisfied and only at $\beta = \beta_{\max}$ otherwise. To prove the theorem, we first express the height y in (1.51) through β by (1.52) and then differentiate the resulting $G(\beta)$ with respect to β . The derivative is given by

$$\frac{dG}{d\beta} = \frac{2\pi R^2}{(1 + \cos \beta)^2} (\gamma_{LV} \sin \beta + \gamma_{SL}^l - \gamma_{wv}), \quad (1.53)$$

showing that the surface energy increases in the non-wetting case (1.49) and decreases otherwise. When G decreases at $\beta = \beta_0$, it will continue decreasing at larger β , with the minimum being reached at $y = y_{\max}$. When G increases at $\beta = \beta_0$, the minimum

Fig. 1.10 Standard vapor–liquid–solid configuration involving surface energies described in the text: the triple phase line (black dots) at the outer periphery of top facet (a) and its stability under random horizontal (b) and vertical (c) shifts

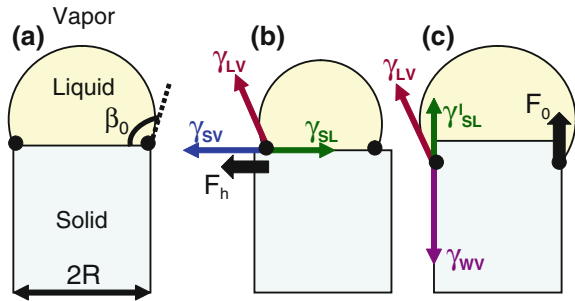
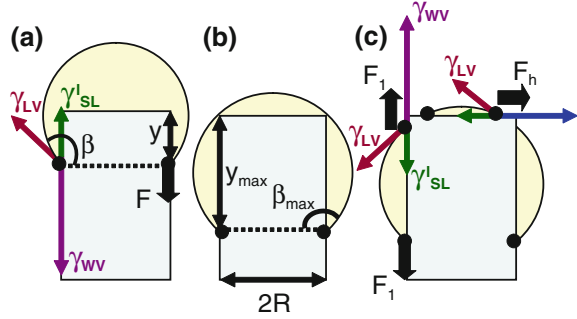


Fig. 1.11 Vapor–liquid–solid wire configuration in the wetting case: unstable configuration with intermediate y (a); system geometry at $y = y_{\max}$ (b) and the directions of surface forces after the droplet is torn apart (c). From geometrical considerations, the maximum of y in spherical geometry is given by $y_{\max} = -2R \cot \alpha n \beta_{\max}$



energy is reached either in the standard configuration with $y = 0$ or at $y = y_{\max}$, depending on whether the value of $G(\beta_0) - G(\beta_{\max})$ is negative or positive.

Surprisingly, the conventional Young's equation on the sidewalls, $\gamma_{WV} = \gamma_{LV} \sin \beta_* + \gamma_{SL}^l$, in the geometry considered relates not to the minimum but to the maximum surface energy. This property follows directly from

$$\left(\frac{d^2 G}{d\beta^2} \right)_{\beta=\beta_*} = \frac{2\pi R^2 \gamma_{LV} \cos \beta_*}{(1 + \cos \beta_*)^2} < 0 \quad (1.54)$$

for any $\beta_* > \pi/2$. The instability of Young's configuration between $y = 0$ and $y = y_{\max}$ is physically explained by the constraint of a fixed liquid volume, with any deviation of contact angle from β_* creating an uncompensated surface force. At $\beta_{\max} < \beta_*$, the standard vapor–liquid–solid configuration with $y = 0$ relates to the global energy minimum. Whenever, $\beta_{\max} > \beta_*$, the two minima of surface energy are separated by the barrier $G(\beta_*)$. The stability of non-wetting configuration is therefore only local.

The next step of system evolution could be the droplet torn apart, as shown in Fig. 1.11c. Let us consider the directions of surface forces in this case. The vertical force acting at the top triple phase line on the wire sidewall, $F_1 = \gamma_{WV} - \gamma_{LV} \sin \beta_{\max} - \gamma_{SL}^l$, is always directed upward in view of (1.50) and $\beta_{\max} > \beta_0$ and. The horizontal force acting upon the triple phase line resting on the top facet, $F_h = \gamma_{SV} + \gamma_{LV} \cos \beta_{\max} - \gamma_{SL}$, returns it back to the outer periphery provided that $\gamma_{SV} > \gamma_{SL} - \gamma_{LV} \cos \beta_{\max}$. This inequality gives the second condition for the stability of droplet at the wire top.

However, as seen from Fig. 1.11c, the force F_1 acting upon the bottom triple phase line on the wire sidewall remains uncompensated and tends to decrease the contact angle β_{\max} . Such force gives rise to further evolution of system morphology, with the droplet losing its spherical geometry. The new, stationary droplet shape should be obtained from the minimization of surface energy functional, a complex problem studied in Chap. 6.

We now turn to the discussion of droplet contact angle β_o in the non-wetting vapor–liquid–solid configuration of Fig. 1.10a. In some works, for example, in [43, 44, 49], it has been assumed that the contact angle could be obtained from the balance of horizontal forces at the triple phase line:

$$\gamma_{SL} = -\gamma_{LV} \cos \beta_o, \quad (1.55)$$

yielding that the droplet is always more than a hemisphere. However, this cannot be proved by the minimization of the total surface energy of the wire-droplet system given by (1.51) at $y = 0$. Indeed, varying the two variables, β and R at fixed V would require a shift of sidewalls. The shift would change the sidewall surface energy $2\pi RL\gamma_{WV}$, which is of course dominant at $L \gg R$. Equation (1.55) can only be obtained from the minimization of the reduced surface energy associated with the droplet:

$$G_0 = \frac{2\pi R^2}{1 + \cos \beta} \gamma_{LV} + \pi R^2 \gamma_{SL}, \quad (1.56)$$

at a constant V given by (1.52) at $y = 0$ [43], where the sidewall energy term is omitted. This should be considered as a hypothesis rather than the rigorous proof of (1.55).

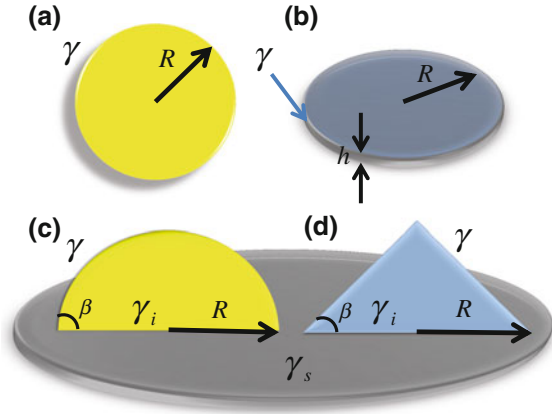
1.5 Formation Energy

Central to nucleation theory is the expression for the free energy of nucleus formation $F_i = \Delta G_i / (k_B T)$ [3, 7–30, 50–53]. Determination of F_i is the core step for construction of any nucleation-condensation model. As discussed already in Sect. 1.2, the macroscopic ($i \gg 1$) change of free energy associated with the formation of a nucleus consisting of i monomers (the formation energy for brevity) always contains the volume term $-(\Delta\mu/k_B T)i$ and the surface energy term. In homogeneous nucleation theory, the $F(i)$ can be thus written down as [3, 7, 9, 50–53]

$$F_i = F_s(i) - (\Delta\mu/k_B T)i = F_s(i) - \ln(\zeta + 1)i, \quad (1.57)$$

where the last expression corresponds to the perfect gas approximation. The entire system is considered to be isothermal, with all nuclei having the same temperature T which is equal to the vapor temperature. This is usually ensured by the presence of a passive gas (in the case of vapor condensation) or the thermostatic effect of the substrate (in the case of surface islands), which is kept constant during the entire growth process. In heterogeneous condensation on the nucleation seeds such as charged ions in gases, (1.57) should be modified to account for the interactions of the liquid with the seed. Particular form of $F_s(i)$ depends on the system geometry, surface energies involved in the transition and, most importantly, the nucleus dimension.

Fig. 1.12 Different shapes of nuclei: 3D liquid droplet (a), 2D surface island on similar substrate (b), spherical cap island (c) and pyramidal island (d) with contact angle β on dissimilar substrate



Let us now consider some typical nucleation scenarios schematized in Fig. 1.12. In the case of 3D spherical droplet of the radius R growing from a supersaturated vapor (Fig. 1.12a), the surface energy contribution is given by $F_s = (\gamma/k_B T) 4\pi R^2$, where γ is the droplet surface energy. Introducing the elementary volume in the liquid phase such that $\Omega i = (4/3)\pi R^3$, we obtain

$$F_s(i) = ai^{2/3}; \quad a = \frac{4\pi\gamma}{k_B T} \left(\frac{3\Omega}{4\pi} \right)^{2/3} = \frac{4\pi\gamma}{k_B T} r_0^2, \quad (1.58)$$

where $r_0 = (3\Omega/4\pi)^{1/3}$ is the interatomic distance in the liquid. For a crystal 3D nucleus growing from vapor, the surface energy term should be re-written as $F_s = (1/k_B T) \sum_k \gamma_k S_k$. This yields the same equation as (1.58), where the constant a sums up the contributions from different crystallographic planes with the corresponding shape constants.

When 2D island of the monolayer height h is formed from an adatom sea or a liquid alloy on the similar substrate (Fig. 1.12b), the surface energy depends on the island shape. The latter is determined by the crystallographic orientation of the substrate and might depend on the growth conditions used. Introducing the linear size R , the island perimeter and surface area can be generally put as $c_1 R$ and $c_2 R^2$, respectively, with the corresponding shape constants c_1 and c_2 . In particular, $c_1 = 2\pi$, $c_2 = \pi$ for circles and $c_1 = 8$, $c_2 = 4$ for squares with side $2R$. The island surface area equals σi , with σ being the elementary surface area. Since homoepitaxial growth should not change the in-plane surface energy, the F_s term corresponds to the formation of lateral surface of monolayer height of the area $c_1 R h$. Therefore,

$$F_s(i) = ai^{1/2}; \quad a = \frac{c_1 \gamma h}{k_B T} \left(\frac{\sigma}{c_2} \right)^{1/2} = \frac{c_1 \gamma h}{k_B T} r_0, \quad (1.59)$$

where γ is the surface energy of the lateral interface in contact with a given environment and $r_0 = (\sigma/c_2)^{1/2}$ is the lattice spacing.

In the case of heteroepitaxy from vapors or liquid alloys, islands can emerge either in 2D or 3D shape. For a 2D island, the lateral surface energy is exactly the same as given by the previous expression, unless it is modified by short-range edge interactions that are not considered here. Besides, the total surface energy contains the in-plane contribution. This is given by $(\gamma_d + \gamma_i - \gamma_s)\sigma i$, where γ_d is the surface energy of the deposited material (created by the nucleation), γ_i is the energy of the deposit-substrate interface (created by the nucleation) and γ_s is the surface energy of the bare substrate (eliminated by the nucleation). Overall, the surface energy of 2D island on the dissimilar substrate is given by

$$F_s(i) = ai^{1/2} + \frac{(\gamma_d + \gamma_i - \gamma_s)\sigma i}{k_B T}. \quad (1.60)$$

Using this in (1.57), it can be re-written in the form

$$F_i = ai^{1/2} - \ln(\zeta + 1)i \quad (1.61)$$

upon the re-normalization of the equilibrium adatom concentration

$$n_{1e}^{eff} \equiv n_{1e} \exp \left[\frac{(\gamma_d + \gamma_i - \gamma_s)\sigma}{k_B T} \right]. \quad (1.62)$$

The latter is modified by the change of in-plane surface energy. Otherwise, the formation energies of 2D islands in homo- and heteroepitaxy are identical.

When a 3D island (liquid or solid) with the base dimension R and contact angle β is formed on a dissimilar substrate (Fig. 1.12c and d), the surface energy change equals

$$F_s(i) = \frac{\gamma}{k_B T} c_1 R^2 + \frac{(\gamma_i - \gamma_s)}{k_B T} c_0 R^2. \quad (1.63)$$

Here, γ is the surface energy of the island, assumed as being constant also for crystal. This property holds for the equivalent lateral facets. The c_1 and c_0 are the shape constants such that $c_1 R^2$ is the lateral surface area and $c_0 R^2$ is the base area of the island. The last term in (1.63) accounts for the change in the in-plane surface energy after nucleation. The island volume amounts to $c_2 R^3$, with c_2 as the corresponding shape constant. For example, $c_0 = \pi$, $c_1 = 2\pi/(1 + \cos \beta)$, and $c_2 = \pi f(\beta)$ for a spherical cap island, with $f(\beta)$ given by (1.40). For a crystal island in the form of pyramid with the rectangular base of side $2R$, $c_0 = 4$, $c_1 = 4/\cos \beta$, and $c_2 = (3/4) \tan \beta$. Using the relationship $\Omega i = c_2 R^3$, (1.63) takes the form

$$F_s(i) = ai^{2/3}; \quad a = \frac{[c_1 \gamma + c_0(\gamma_i - \gamma_s)]}{k_B T} \left(\frac{\Omega}{c_2} \right)^{2/3}. \quad (1.64)$$

A more complex case of a lattice mismatched substrate, where the mismatch-induced strain modifies the volume energy depending on the island shape and the aspect ratio, will be considered in Chap. 3.

Summarizing, the surface energy contribution can be put as $ai^{2/3}$ for a 3D nucleus and $ai^{1/2}$ for a 2D island in all the cases considered. We can therefore present the macroscopic formation energy F_i in the form [52]

$$F_i = ai^{(d-1)/d} - \ln(\zeta + 1)i, \quad (1.65)$$

where $d = 2, 3$ is the space dimension of the nucleus. The first, positive contribution describes the energetically unfavorable process of the formation of new surfaces, with coefficient a being proportional to the characteristic surface energy in thermal units. This coefficient is always much larger than one, showing that the surface is stable against thermal fluctuations. For example, $a = 9.6$ in the case of water condensation at room temperature. In the case of heterogeneous condensation of vapor on the charged ions ($d = 3$), (1.65) is modified as [9]

$$F_i = ai^{2/3} - \ln(\zeta + 1)i + ci^{-1/3}, \quad (1.66)$$

where $c = q^2(\varepsilon_v^{-1} - \varepsilon_l^{-1})/(2k_B Tr_0)$, q is the electrical charge of the ion, and $\varepsilon_v, \varepsilon_l$ are the dielectric constants in the gas-vapor system and in the liquid, respectively.

The function $F(i)$ defined by (1.65) reaches its maximum

$$F(\zeta) \equiv F[i_c(\zeta)] = \frac{(d-1)^{d-1}}{d^d} \frac{a^d}{\ln^{d-1}(\zeta + 1)} = \frac{a}{d} i_c^{\frac{d-1}{d}} \quad (1.67)$$

at the critical size

$$i_c(\zeta) = \left[\frac{(d-1)a}{d \ln(\zeta + 1)} \right]^d. \quad (1.68)$$

The quantity $F(\zeta)$ is the nucleation barrier at a given supersaturation. The critical nucleus is in unstable equilibrium with a metastable phase; the nuclei with $i > i_c$ tend to grow, while smaller nuclei with $i < i_c$ tend to evaporate. Of course, there is an almost zero probability that i_c is an integer. The half-width of the near-critical region Δi_c , defined by $(|F''(i_c)|/2) \Delta i_c^2 = 1$, is readily obtained as

$$\Delta i_c = d \left(\frac{2}{(d-1)a} \right)^{1/2} i_c^{\frac{d+1}{2d}}. \quad (1.69)$$

If the critical size is large enough, (1.68), (1.69) can be used for the charged droplets as well. However, in heterogeneous nucleation, the formation energy has a minimum at small i , corresponding to the energetically preferred stable state. In this case, the nucleation barrier is modified to $\Delta F(\zeta) = F(\zeta) - F_{\min}(\zeta)$.

Let us now discuss a very important question of quasi-equilibrium distribution normalization and the corresponding size-independent corrections to the macroscopic formation energy [3, 7, 54]. Such modifications do not change (1.68) and (1.69) but do influence the nucleation barrier and related values. The quasi-equilibrium concentration of nuclei with i atoms n_i^{eq} is given by the Boltzmann exponent of the formation energy [38]. When vapor is at the concentration n_1 , the n_i^{eq} is given by [7, 9]

$$n_i^{eq} = n_1 \exp(-F_i). \quad (1.70)$$

It should be noted here that the quasi-equilibrium distribution n_i^{eq} relates to a metastable vapor, while the global equilibrium is reached at $n_1 = n_1^{eq} \equiv n_{1e}$, that is, at zero supersaturation. It is easily seen that this equation is self-inconsistent when F_i is given by (1.65): since $F_1 \neq 0$, it does not give correctly the monomer concentration at $i = 1$. Kashchiev [7] proposed to use $F_i - F_1$ instead of F_i for the formation energy, which modifies (1.70) to

$$n_i^{eq} = n_1 \exp[-(F_i - F_1)]. \quad (1.71)$$

This equation is self-consistent at $i = 1$. The corresponding corrections to the macroscopic (1.65), (1.67) are given by

$$F_i = a[i^{(d-1)/d} - 1] - \ln(\zeta + 1)(i - 1); \quad (1.72)$$

$$F(\zeta) \equiv F[i_c(\zeta)] = \frac{(d-1)^{d-1}}{d^d} \frac{a^d}{\ln^{d-1}(\zeta + 1)} - a + \ln(\zeta + 1). \quad (1.73)$$

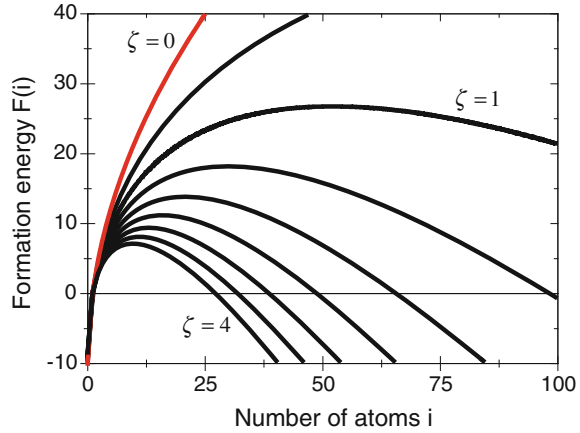
In view of $a \gg 1$, such a correction will lead to increasing the size distribution normalization by the orders of magnitude.

Long ago, Lothe and Pound [55] proposed another correction to the formation energy originating from the entropy factor in distributing n_1 monomers over n_0 sites in the lattice (where $n_0 = 1/\Omega$ for 3D and $n_0 = 1/\sigma$ for 2D lattice):

$$F_i = ai^{(d-1)/d} - \ln(\zeta + 1)i + \ln(n_1/n_0). \quad (1.74)$$

The logarithmic term change the pre-exponential factor of the equilibrium distribution from n_1 to n_0 . In view of $n_1/n_0 \ll 1$, the normalization increases again by the orders of magnitude. Although we do not see any reasonable justification for the Lothe-Pound factor in the general case, such a correction is often used in modeling adatom nucleation and thin film growth [3]. Together with the F_1 correction as given by (1.70), (1.74) gives the result which is obviously incorrect at $i = 1$. However, without the F_1 term, the large factors $\exp(a)/(\zeta + 1)$ and $n_0/n_1 = 1/[\theta_{1e}(\zeta + 1)]$ might be of the same order. Overall, the problem of distribution normalization in the macroscopic theory requires special attention. Truly microscopic approaches are needed to describe correctly the formation energy of small clusters consisting of only

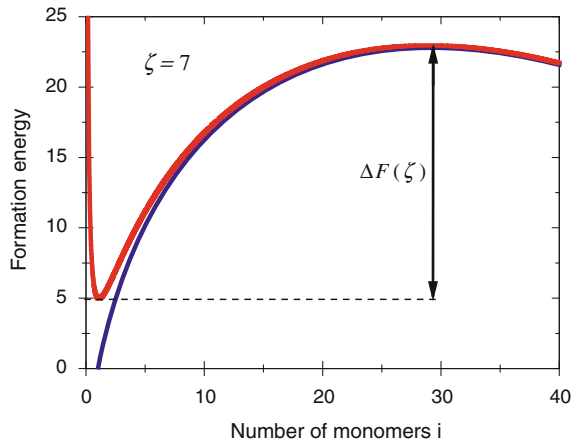
Fig. 1.13 Formation energy of 2D island at $a = 10$ and different supersaturations from 0 to 4



a few monomers. Surprisingly, the problem simplifies in the case of nucleation in open systems due to a special type of self-consistency between the external material influx and the material sink by nucleation, as described in detail in Chap. 2.

Figure 1.13 shows the formation energy of 2D island at the fixed $a = 10$ and different supersaturations, obtained from (1.72). The equilibrium case at $\zeta = 0$ relates to infinite nucleation barrier where the transition is thermodynamically forbidden. Increasing supersaturation from 0.5 to 4 leads to decrease of the critical number of monomers from 55 to 11, while the nucleation barrier decreases from 27 to 7. Further increase of supersaturation will break the possibility of using the macroscopic approach. We note, however, that if supersaturation increases gradually due to a material influx into the system or, more generally, by smoothly changing the macroscopic parameters, supersaturation would not increase to these high val-

Fig. 1.14 Formation energies of 3D droplets in homogeneous and heterogeneous cases at $\zeta = 7$, $\Delta F(\zeta)$ showing the decreased barrier for heterogeneous nucleation



ues. Rather, it would reach a maximum at a certain stage due to a dynamic balance between the material influx and the monomer sink caused by nucleation and growth of embryos. This maximum supersaturation would correspond to a high enough nucleation rate which can outweigh the material influx, but is still low enough to be reasonably described within the macroscopic theory.

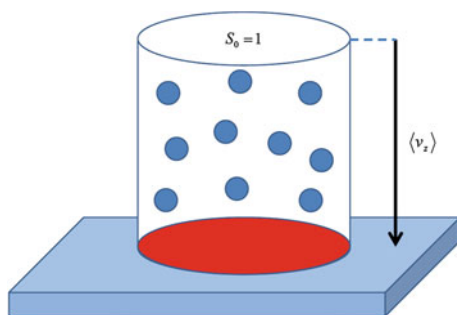
In Fig. 1.14, we show how the condensation seeds decrease the nucleation barrier at a given supersaturation value. As discussed later on, the nucleation rate, the value giving the number of irreversibly growing nuclei per unit volume per unit time, is extremely sensitive to supersaturation. The decrease of ζ by only a few percent results in decreasing the nucleation rate by the order of magnitude. This naturally leads to a certain threshold value of supersaturation in a given material system, below which the nucleation process is too slow to be observed on a realistic time scale. The existence of nucleation seeds such as charged ions in 3D gas–vapor systems or surface steps, kinks or chemical impurities on a 2D surface can therefore significantly decrease this threshold value.

1.6 Adsorption and Thin Films

In many practical applications of nucleation theory such as modeling the growth properties of nanostructures synthesized by different epitaxy techniques, we deal with metastable adatom systems, surface islands and layers. An “ideal” substrate surface without defects, steps or chemical impurities can be treated as a 2D lattice of a given geometry that can accommodate atoms in the adsorption sites. The 2D lattice gas is a good model to describe the monolayer film on a crystal surface in the case of strongly localized adsorption. The film is usually grown from vapor or, more generally, from a gaseous system characterized by the deposition rate (or the arrival rate) I ($1/\text{cm}^2 \text{ s}$) onto the substrate [3, 56, 57].

In the case of vapor phase with pressure P and temperature T_v above the surface, the arrival rate can be calculated from the gas kinetic theory [38]. As shown in Fig. 1.15, the number of vapor molecules arriving onto the unit surface area per unit

Fig. 1.15 To the calculation of vapor flux impinging the elementary area $S_0 = 1$



time is given by $I = n_v \langle v_z \rangle$. Here, $\langle v_z \rangle$ is the averaged component of molecule speed in the direction normal to the substrate. The latter can be easily found from the Maxwell distribution at temperature T_v :

$$\langle v_z \rangle = \left(\frac{m}{2\pi k_B T_v} \right)^{1/2} \int_0^\infty dv v \exp \left(-\frac{mv^2}{2k_B T_v} \right) = \sqrt{\frac{k_B T_v}{2\pi m}}. \quad (1.75)$$

with m as the molecule mass. The integration over speeds is performed from zero to infinity, because the molecules with $v_z < 0$ fly away from the surface. The vapor flux can be therefore presented in two equivalent forms

$$I = \sqrt{\frac{k_B T_v}{2\pi m}} n_v = \frac{P}{\sqrt{2\pi m k_B T_v}} \quad (1.76)$$

by using the perfect gas equation of state $P = n_v k_B T_v$.

When the vapor and the substrate temperatures equal each other, the gaseous phase is in equilibrium with the film having the occupation θ (called the coverage in the case of adsorbed surface layers) provided that $\mu_g = \mu(\theta)$, where $\mu(\theta)$ is the lattice gas chemical potential defined by (1.6). The chemical potential of gaseous phase is given by $\mu_g/k_B T = \ln(P/P_0) = \ln(I/I_0)$, with certain constants P_0 and I_0 . We thus arrive at the Fowler-Guggenheim adsorption isotherm [58]

$$\ln \left(\frac{I}{I_0} \right) = -\varphi\theta + \ln \left(\frac{\theta}{1-\theta} \right); \quad \frac{I}{I_0} = \frac{\theta}{1-\theta} \exp(-\varphi\theta). \quad (1.77)$$

For very small $\theta \ll 1$, (1.77) is reduced to the Henry's law stating that the coverage is proportional to the vapor flux:

$$\theta = I/I_0. \quad (1.78)$$

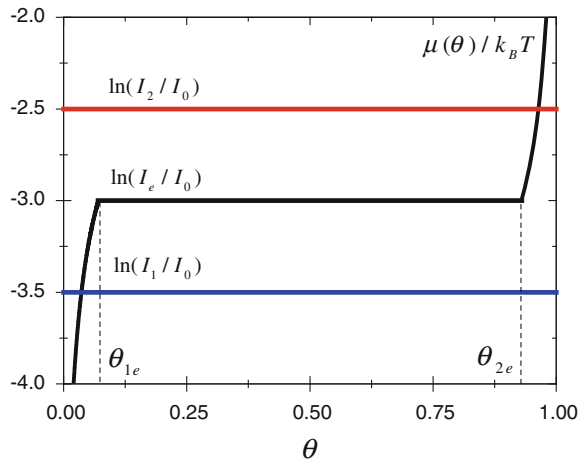
For an ideal adsorbate with no attractive interactions ($\varphi = 0$), (1.77) gives the Langmuir isotherm

$$\theta = \frac{I/I_0}{1 + I/I_0} \quad (1.79)$$

for any θ between zero and one.

The adsorption isotherm of non-ideal monolayer adsorbate given by (1.77), describes three principally different equilibrium states in the adsorbate-vapor system at $T < T_c$ [38, 59, 60], plotted in Fig. 1.16. When $\ln(I/I_0) < -\varphi/2 = \mu_e/k_B T$, the equilibrium state relates to a sub-monolayer coverage, with $\theta_0 \ll 1$ at temperatures well below T_c . The vapor at $\ln(I/I_0) > -\varphi/2$ is in equilibrium with a dense adsorbate, whose coverage rapidly tends to one at low temperatures. The unique situation with $\ln(I_e/I_0) = -\varphi/2$ corresponds to the coexistence of the three phases: vapor with the equilibrium flux I_e , and two adsorbate phases with the equilibrium coverages θ_{1e} and θ_{2e} . When θ_{1e} and θ_{2e} are close to zero and one, respectively, we

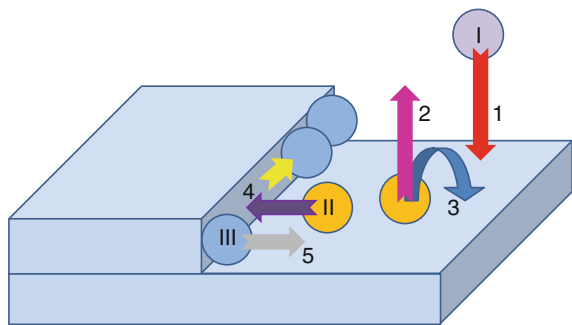
Fig. 1.16 Three possible equilibrium states in the adsorbate-vapor system: stable adatom system with $\theta_0 \ll 1$ at $I/I_0 < \mu_e$, stable monolayer at $I/I_0 > \mu_e$ and coexistence of vapor with two adsorbate phases having the equilibrium densities θ_{1e} and θ_{2e} at $I_e/I_0 = \mu_e$. The $\mu(\theta)$ curve corresponds to $\varphi = 6$, the horizontal part corresponds to the density discontinuity



deal with a dilute adatom sea which is in equilibrium with vapor (due to a dynamic balance of adsorption and desorption processes) and, at the same time, coexists with the monoatomic surface step. The condition for the film growth clearly yields $I > I_e$, the inequality which should hold in any epitaxy process. In this case, supersaturation of the adatom sea will increase gradually with time due to deposition until it hits the threshold value necessary to initiate the film growth. The value of critical supersaturation depends on whether the substrate is planar or vicinal. In the former case, the surface steps should be created by nucleation, while in the latter case they are present initially.

Let us now briefly consider the most important elementary processes on a solid surface [3], illustrated in Figs. 1.17 and 1.18. The first process shown in Fig. 1.17 is the physical adsorption with probability χI per unit time per unit area. The χ is the adsorption coefficient showing which percentage of atoms from the impinging vapor flux actually becomes adatoms. In chemical deposition methods using precursors to deliver the required growth species onto the surface, χ is defined by the pyrolysis

Fig. 1.17 1 adsorption; 2 desorption; 3 surface diffusion; 4 incorporation to monoatomic step (2D condensation); 5 2D evaporation from the step. *I* denotes the vapor atom, *II* is the adatom on a planar terrace and *III* is the incorporated adatom



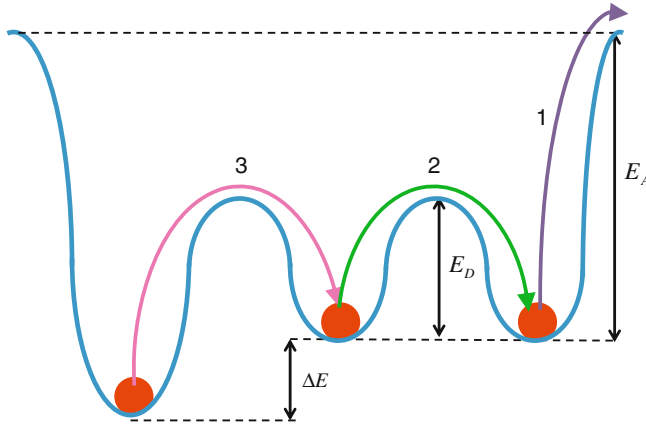


Fig. 1.18 Energy profile of a solid surface and the activation energies of different processes: E_A —desorption (1); E_D —surface diffusion (2); ΔE —escape from a kink (3)

efficiency at a given substrate temperature [61]. In molecular beam epitaxy [62, 63], it is primarily determined by the source temperature and the incident angle of the beam to the substrate. Usually, χ is very close to one, unless the beam approaches the glazing incidence. The second process shown in Fig. 1.17 is the desorption whose probability is characterized by the mean adatom lifetime on the surface before re-evaporation

$$\tau_A = \nu_A^{-1} \exp\left(\frac{E_A}{k_B T}\right). \quad (1.80)$$

Here, E_A is the activation energy for desorption (see Fig. 1.18), and ν_A is the pre-exponential factor which is of the order of thermal oscillation frequency of the lattice (10^{11} – 10^{13} s $^{-1}$).

Whenever $I < I_e$ and, therefore, $n_1 < n_{1e}$, the adatom concentration obeys the simple kinetic equation

$$\frac{dn_1}{dt} = \chi I - \frac{n_1}{\tau_A}. \quad (1.81)$$

Obviously, n_1 tends to its maximum value $\chi I \tau_A$ with the relaxation time τ_A :

$$n_1(t) = \chi I \tau_A \left[1 - \exp\left(-\frac{t}{\tau_A}\right) \right] \quad (1.82)$$

Comparing (1.81) and (1.78) we obtain $I_0 = 1/(\chi \sigma \tau_A)$, where σ is the area of adsorption site.

The third elementary process in Fig. 1.17 is the surface diffusion of adatoms. In the case of strongly localized adsorbates, adatoms oscillate near the points of minima of the surface potential and jump to the neighboring sites. Probability of the jump per unit time is given by

$$t_D = \nu_D^{-1} \exp\left(\frac{E_D}{k_B T}\right). \quad (1.83)$$

Here, E_D is the activation energy for diffusion (see Fig. 1.18), and ν_D is the corresponding pre-exponential factor. The diffusion coefficient can be defined as

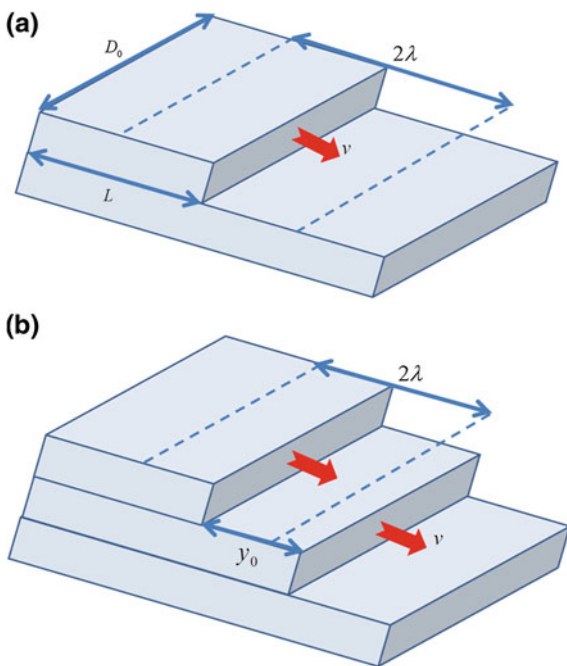
$$D = \frac{l_D^2}{\xi t_D}, \quad (1.84)$$

where l_D is the length of diffusion jump ($l_D^2 \cong \sigma$) and ξ is the lattice coordination number. The adatom diffusion length is the average square distance passed by the adatom on a bare substrate before it desorbs:

$$\lambda = \sqrt{D\tau_A}. \quad (1.85)$$

Usually, E_A is at least two times larger than E_D . Since both energies are much larger than $k_B T$, the adatom can make many diffusion jumps before its desorption. Equation (1.85) is sometimes used with the effective lifetime limited by incorporation into the surface steps or the boundaries of growing islands rather than just by desorption. In this case, the values of τ_A and λ depend on the surrounding and can no longer be attributed to a single adatom.

Fig. 1.19 Growth rate of a single step (a) and an echelon of steps (b)



Let us now see how a straight step grows from a supersaturated adatom “sea”. As shown in Fig. 1.19a, a single step of the width $D_0 = \text{const}$ is fed from the terrace area $2D_0\lambda$. Assuming that all $2\chi ID_0\lambda$ atoms arriving from vapor to this collection area per unit time are subsequently attached to the step (process 4 in Fig. 1.17), and taking the reverse flux from the step to the terrace (process 5 in Fig. 1.17) in the form $2\chi I_e D_0\lambda$, the growth rate $v_s = dL/dt$ of the step is obtained as

$$v_s = 2\sigma\lambda\chi I_e \Phi. \quad (1.86)$$

Here, $\Phi = I/I_e - 1$ is the vapor supersaturation with respect to the surface. When rather than a single step, the echelon of steps is growing separated by the spacing y_0 (Fig. 1.19b), the steps will compete for the diffusion flux from the terraces. Now, a function of $y_0/(2\lambda)$ must enter the growth equation. This function, first derived by Burton, Cabrera and Frank [63], is given by $\tanh(y_0/2\lambda)$, modifying the previous equation to

$$v_s = 2\sigma\lambda\chi I_e \tanh\left(\frac{y_0}{2\lambda}\right) \Phi. \quad (1.87)$$

Obviously, the growth rate decreases toward smaller y_0 and is reduced to (1.86) at $y_0/(2\lambda) \gg 1$.

Whenever the actual adatom concentration on the terrace is smaller than $\chi I\tau_A$, which usually happens due to nucleation of 2D islands on the terrace, the Φ in the above equations should be changed to the adatom supersaturation $\zeta = n_1/n_{1e} - 1$. In particular, in view of $\chi I_e = n_{1e}/\tau_A$, (1.86) should be re-written as

$$v_s = \frac{2\sigma\lambda n_{1e}}{\tau_A} \zeta. \quad (1.88)$$

Equation (1.88) for a straight step can be used to obtain a simplified formula for the growth rate of 2D island whose size is much larger than critical, where the curvature effects can be neglected. Indeed, the growth equation can be re-arranged as $\sigma^{-1} dS/dt = di/dt = P_{isl}(\lambda n_{1e} \zeta)/\tau_A$, where S is the island area, i is the number of atoms in the island and P_{isl} is the perimeter. Adatoms of the second layer are not taken into account here. For a circular island with $P_{isl} = 2\pi R$, the growth rate writes down as

$$\frac{di}{dt} = \frac{2\pi R D n_{1e}}{\lambda} \zeta. \quad (1.89)$$

The island growth rate in this approximation is proportional to R and, therefore, to $i^{1/2}$.

If we formally put $\lambda = l_D$, thus accounting only for such adatoms that can reach the island boundary in one diffusion jump, and use (1.84) for D together with the relationship $\pi R^2 = \sigma i$, (1.89) takes the well-known form [3, 65, 66]

$$\frac{di}{dt} \cong \frac{2\sqrt{\pi\sigma} l_D}{\xi t_D} n_{eq} i^{1/2} \zeta = \frac{2i^{1/2}}{\tau} \zeta. \quad (1.90)$$

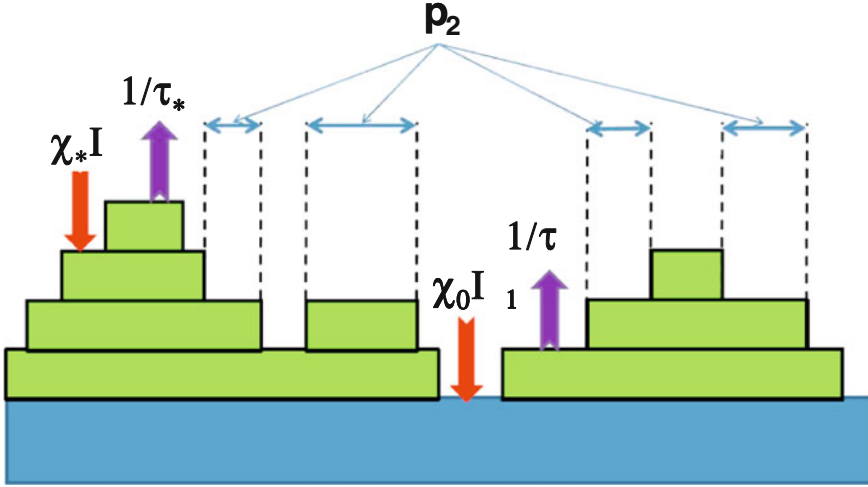


Fig. 1.20 BET model of multilayer adsorption with the parameters described in the text

Here, by definition, τ is the characteristic time of island growth which is of the order of t_D/θ_{1e} . Equation (1.90) pertains only if the diffusion length is much smaller than the island linear size. More general expressions for the growth rate of 2D islands will be given in the next section.

The approach presented above is principally limited to the monolayer adsorption. To access the case of thicker films, we consider the multilayer surface structure shown in Fig. 1.20. Different layers are labeled by indices $i = 1, 2, 3 \dots$; the index $i = 0$ relates to the surface. Each layer is characterized by the coverage θ_i giving the percentage of the surface area covered by this layer (yielding $\theta_0 \equiv 1$). In absence of vacancies and overhangs in the film, the quantities

$$p_0 = 1 - \theta_1; \quad p_1 = \theta_1 - \theta_2; \quad \dots \quad p_i = \theta_{i-1} - \theta_i \dots \quad (1.91)$$

are the probabilities that the layer i is exposed to the vapor. Kinetic balance equations for p_i can be written down as

$$\begin{aligned} \frac{dp_0}{dt} &= -\chi_0 \sigma I p_0 + \frac{p_1}{\tau_1}, \quad i = 0; \\ \frac{dp_i}{dt} &= \chi_{i-1} \sigma I p_{i-1} - \frac{p_i}{\tau_i} - \chi_i \sigma I p_i + \frac{p_{i+1}}{\tau_{i+1}}, \quad i = 1, 2, 3 \dots \end{aligned} \quad (1.92)$$

The quantities χ_i and τ_i are the adsorption coefficients on the surface of layer i and the characteristic desorption times from layer i , respectively. The adsorption on the surface of layer $i - 1$ must be compensated by the desorption from layer i in equilibrium:

$$p_i = \chi_{i-1} \sigma I \tau_i p_{i-1} \quad , \quad i = 1, 2, 3, \dots, \quad (1.93)$$

where we write p_i instead of p_i^{eq} for brevity.

Following the idea of Brunauer, Emmett, Teller [67], we now assume that the characteristics of all the layers beginning from the second one are identical. However, the first layer is different due to the influence of a dissimilar substrate surface: $\chi_0 \neq \chi_1 = \chi_2 = \chi_3 = \dots \equiv \chi_*$; $\tau_1 \neq \tau_2 = \tau_3 = \tau_4 = \dots \equiv \tau_*$. Introducing the normalized vapor flux b and the parameter c accounting for the difference of the first and the upper layers by definitions

$$b = \chi_* \sigma I \tau_*; \quad c = \frac{\chi_0 \tau_1}{\chi_* \tau_*}, \quad (1.94)$$

(1.93) simplifies to

$$p_i = cb^i p_0. \quad (1.95)$$

The probabilities p_i are normalized to one from geometrical considerations. The mean thickness of multilayer adsorbate h (measured in the units of a monolayer height) is the statistical average of i with probabilities p_i . Therefore,

$$\sum_{i=0}^{\infty} p_i = 1; \quad h = \sum_{i=0}^{\infty} i p_i. \quad (1.96)$$

Inserting (1.95) into (1.96) and performing the respective summation of geometrical progressions, one obtains the known two-parametric Brunauer-Emmett-Teller (BET) isotherm [67]:

$$h = \frac{cb}{(1-b)(1-b+cb)}. \quad (1.97)$$

Graphs of the film thickness h versus b at different c are plotted in Fig. 1.21. The case of $c = 1$ corresponds to the identical characteristics in the first and the upper layers, that is, the adsorption on the similar substrate. When $c \ll 1$, the film does not wet the surface due to a small adsorption coefficient or an enhanced desorption. The thickness of a non-wetting film is the lowest at given vapor pressure. The case of $c \gg 1$ corresponds to a good wetting, where the first layer forms easily and the total thickness is limited by formation of the upper layers. The film thickness at a given pressure is much higher than in the previous cases. Since the thickness increases monotonously with the flux, the BET isotherm does not give any phase transition, i.e., describes a perfect multilayer adsorbate. Some generalizations of the BET model have been studied, for example, in [31], where the attractive interactions are introduced within the frame of the mean field theory in each layer and between the layers, while the entire adsorption process is studied kinetically. More details on the kinetic lattice gas models for adsorption phenomena can be found, for example, in [68–70].

1.7 Growth Rates

Growth rate of a nucleus depends strongly on its dimension (2D or 3D) as well as on the dimension and characteristics of supersaturated environment. We start the analysis with a simplified picture shown in Fig. 1.22. The nucleus considered is assumed to be a disc or a sphere of radius R fed from a supersaturated 2D or 3D environment, respectively. The radius is assumed as being sufficiently larger than the critical radius. This allows us to neglect the curvature effects. We thus consider the growth rates of essentially super-critical nuclei so that the derivative of formation energy defined by (1.65) with respect to i tends to $-\ln(\zeta + 1)$. The vapor concentration equals n_1 at the distance Λ from the interface, and decreases towards the interface due to a diffusion flux onto the nucleus. The equilibrium concentration n_{1e} must be reached at the interface. The quantity Λ therefore plays a role of the characteristic length of spatial inhomogeneity in supersaturated environment.

Stationary diffusion equation with the corresponding boundary conditions

Fig. 1.21 BET isotherms at different c

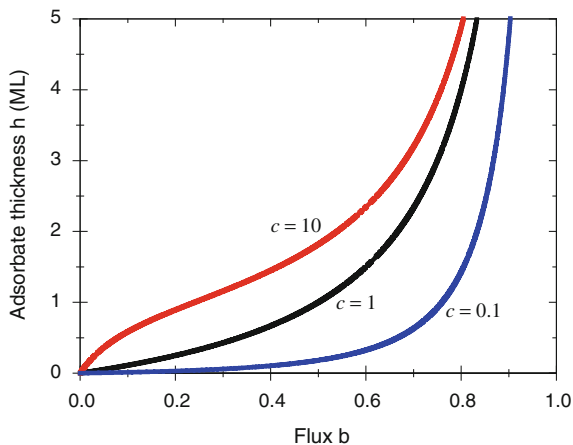
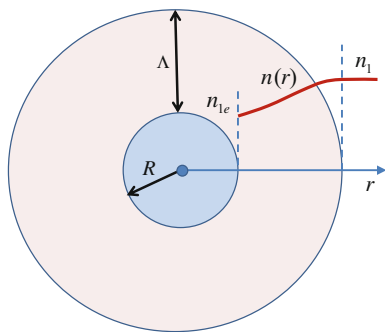


Fig. 1.22 Diffusion-induced growth of nucleus with the vapor concentration decreasing from n_1 at distance Λ to n_{1e} at the interface



$$\Delta n(r) = 0; \quad n(r = R) = n_{1e}; \quad n(r = R + \Lambda) = n_1 \quad (1.98)$$

describes the concentration profiles in absence of external fluxes; Δ denotes the Laplace operators in 2D ($d = 2$) or 3D ($d = 3$) space. Solutions to this equation are given by

$$n(r) = n_{1e} + \frac{(n_1 - n_{1e})}{\ln(1 + \Lambda/R)} \ln\left(\frac{r}{R}\right), \quad d = 2; \quad (1.99)$$

$$n(r) = n_{1e} + (n_1 - n_{1e}) \left(1 + \frac{R}{\Lambda}\right) \left(1 - \frac{R}{r}\right), \quad d = 3. \quad (1.100)$$

The corresponding material fluxes onto the surface

$$\frac{di}{dt} = D2\pi R \left. \frac{dn}{dr} \right|_{r=R}, \quad d = 2; \quad (1.101)$$

$$\frac{di}{dt} = D4\pi R^2 \left. \frac{dn}{dr} \right|_{r=R}, \quad d = 3, \quad (1.102)$$

give the diffusion-induced growth rates. Straightforward calculation leads to the following results

$$\frac{di}{dt} = \frac{2\pi D n_{eq} \zeta}{\ln(1 + \Lambda/R)}; \quad d = 2; \quad (1.103)$$

$$\frac{di}{dt} = 4\pi D n_{eq} \zeta R \left(1 + \frac{R}{\Lambda}\right); \quad d = 3. \quad (1.104)$$

Despite its simplicity, our model illuminates well two major features. First, the growth rates of super-critical nuclei are proportional to the supersaturation, yielding the phase coexistence at $\zeta = 0$, growth at $\zeta > 0$ and evaporation at $\zeta < 0$. Second and less obvious, it is seen that the growth rates are proportional to the perimeter in 2D case and surface area in 3D case at $\Lambda \ll R$, where the nucleus does not disturb significantly the spatial homogeneity of the gas–vapor environment. This mode, corresponding to $di/dt \propto i^{1/2}$ in 2D and $di/dt \propto i^{2/3}$ in 3D space, is called the ballistic growth regime [3, 10, 15, 17, 50–53]. The opposite case of $\Lambda \gg R$, where the inhomogeneity length is much larger than the particle linear dimension, relates to $di/dt \propto 1/\ln(\Lambda/R)$ in a 2D system. This weak logarithmic dependence at $\Lambda/R \gg 1$ can often be neglected, yielding an almost size-independent growth rate of small enough islands. The growth rate of 3D island in the same limit is proportional to $i^{1/3}$. Such a growth is said to proceed in the diffusion regime [50–53, 69].

When the impingement and desorption processes are included, the diffusion equation for the adatom concentration around a 2D island writes down as

$$\lambda^2 \Delta n + n_{1\infty} - n = 0. \quad (1.105)$$

Here, λ is the adatom diffusion length and $n_{1\infty}$ is the concentration far away from the island. General solution to this equation is given by

$$n(r) = n_{1\infty} + c_1 I_0(r/\lambda) + c_2 K_0(r/\lambda), \quad (1.106)$$

with $I_0(z)$ and $K_0(z)$ as the modified Bessel functions of zero order, and the two constants determined by the boundary conditions. Since $I_0(z)$ increases at large z , we must put c_1 to zero to ensure the correct behavior far away from the island. Boundary condition at the interface remains the same as in (1.98), yielding

$$n(r) = n_{1\infty} - (n_{1\infty} - n_{1e}) \left[\frac{K_0(r/\lambda)}{K_0(R/\lambda)} \right]. \quad (1.107)$$

Calculation of the diffusion flux onto the island by means of (1.101) readily gives

$$\frac{di}{dt} = \frac{2\pi R D n_{1e} \zeta}{\lambda} \frac{K_1(R/\lambda)}{K_0(R/\lambda)}, \quad (1.108)$$

where $\zeta = n_{1\infty}/n_{1e} - 1$ and $K_1(z)$ is the modified Bessel function of the first order. Compared to (1.89), this expression contains the ratio of the two Bessel functions. The latter tends to one at $R/\lambda \gg 1$ and to $\lambda/[R \ln(\lambda/R)]$ at $R/\lambda \ll 1$, reducing (1.108) to (1.89) and

$$\frac{di}{dt} = \frac{2\pi D n_{1e}}{\ln(\lambda/r)} \zeta, \quad (1.109)$$

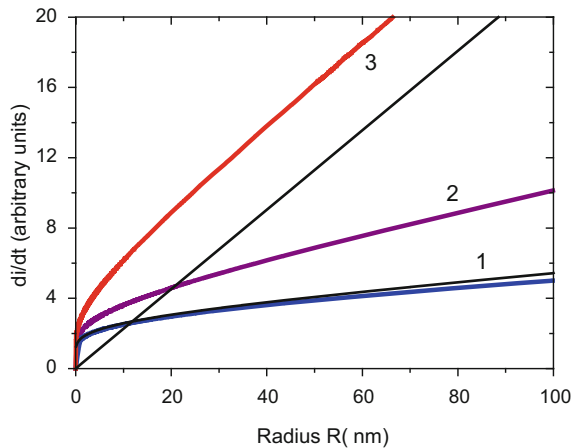
respectively. The last expression is identical to (1.103) at $R/\Lambda \ll 1$ and $\Lambda = \lambda$. The characteristic scale of spatial inhomogeneity thus appears to be exactly equivalent to the adatom diffusion length, which is indeed a natural and well anticipated result.

Figure 1.23 shows the growth rates obtained from (1.108) with different diffusion lengths at otherwise identical parameters. Black lines are the approximations given by (1.109) and (1.89). It is clearly seen that the logarithmic approximation works very well everywhere at large $\lambda = 800$ nm, even if the radius is smaller than λ . The radius dependence of the growth rate is indeed weak. The linear approximation at small $\lambda = 50$ nm predicts correctly the slope angle, but is shifted downward compared to the exact expression. Therefore, (1.108) at $R/\lambda \gg 1$ can be well fitted by a linear function with a certain additive correction.

For a spherical droplet in the ballistic growth regime in 3D space, the condensation rate equals the vapor flux impinging the entire droplet surface $S = 4\pi R^2$ per unit time, multiplied by the corresponding adsorption coefficient at the surface: $W_i^+ = \chi I S$. In isothermal conditions, the I is given by (1.76) at $T_v = T$ and $n_v = n_1$, because the vapor molecules now play the role of condensing monomers. This yields

$$W_i^+ = 4\pi R^2 \chi n_1 \sqrt{\frac{k_B T}{2\pi m}} = \frac{3i^{2/3}(\zeta + 1)}{\tau}. \quad (1.110)$$

Fig. 1.23 Dependences of the growth rate on R at different $\lambda = 800$ nm (curve 1), 200 nm (curve 2), and 50 nm (curve 3). Black lines show approximations described in the text



The kinetic time constant τ , defined as $\tau^{-1} = (4\pi\Omega^2/3)^{1/3} \chi n_{1e} (k_B T / 2\pi m)^{1/2}$, gives the characteristic time of droplet growth. The evaporation rate of super-critical droplets W_i^- must equal the condensation rate at $\zeta = 0$. The growth rate of super-critical droplets is therefore given by

$$\frac{di}{dt} = \frac{3i^{2/3}\zeta}{\tau}. \quad (1.111)$$

This expression is also valid for a crystal nucleus growing from a supersaturated vapor, where only the constant τ is changed.

The ballistic growth regime in 3D space holds as long as the nucleus does not disturb the gas–vapor environment. This is ensured by the following inequality:

$$\frac{\chi R}{l} \ll 1, \quad (1.112)$$

where l is the free path length of the vapor molecules. For larger nuclei, the growth proceeds in the diffusion regime. Generalized expression accounting for both mechanisms as well as the transition between them can be obtained in the form [69]

$$\frac{di}{dt} = \frac{3i^{2/3}\zeta}{\tau} \frac{1}{1 + (i/i_l)^{1/3}}. \quad (1.113)$$

Here, i_l denotes the number of molecules in the droplet having the radius l/χ . Obviously, this expression has the same asymptotic behaviors as those given by (1.104).

As follows from our analysis, the growth rates of 2D islands and 3D droplets obey the scaling law $di/dt \propto W_i^+ \propto i^\alpha$ in most cases, where the exponent α depends on the space dimensions of the metastable system ($d' = 2, 3$) and the nucleus ($d = 2, 3$), as well as on the mechanisms of mass transport into the nucleus. Let us now briefly

Table 1.2 Schematization of growth scenarios and growth indices for different systems

No	System description	d'	d	α	m	Invariant size ρ
1	Thin film growth at low temperatures	3	2	0	1	i
2	Growth of 2D islands from 2D adatom sea, ballistic regime	2	2	1/2	2	$i^{1/2}$
3	Growth of 2D islands from 2D adatom sea, diffusion regime	2	2	0	1	i
4	Condensation of 2D island from 3D environment	3	2	1	∞	$\ln i$
5	Growth of 3D islands from 2D system, ballistic regime	2	3	1/3	3/2	$i^{2/3}$
6	Growth of 3D islands from 2D system, diffusion regime	2	3	0	1	i
7	Condensation of 3D droplets from 3D vapor, ballistic regime	3	3	2/3	3	$i^{1/3}$
8	Condensation of 3D droplets from 3D vapor or liquid, diffusion regime	3	3	1/3	3/2	$i^{2/3}$

discuss other relevant growth scenarios [50]. As follows directly from (1.92) at i -independent χ_i and $\tau_i \rightarrow \infty$, the low temperature growth of multilayer thin film without surface diffusion and desorption proceeds at $\alpha = 0$. Growth of 3D surface islands from a 2D metastable system ($d' = 2, d = 3$) relates to $\alpha = 1/3$ in the ballistic regime (the case of the Stranski-Krastanow quantum dots [25]) and $\alpha = 0$ in the diffusion regime. A more exotic case of surface island fed from a vapor or liquid phase though its surface but growing in a 2D form ($d' = 3, d = 2$), corresponds to $\alpha = 1$.

Different growth regimes are summarized in Table 1.2, where the growth index m is introduced by definition

$$m = \frac{1}{1 - \alpha}. \quad (1.114)$$

As discussed, the exponent α usually ranges from zero to one, yielding $1 \leq m \leq \infty$. The α values between 0 and 2/3 relate to $1 \leq m \leq 3$. At $\alpha < 1$, we write down the condensation rate in two equivalent forms:

$$W_i^+ = \frac{(\zeta + 1)}{(1 - \alpha)\tau} i^\alpha = \frac{m(\zeta + 1)}{\tau} i^{(m-1)/m}. \quad (1.115)$$

At $\alpha = 1$, we do not introduce the factor $1 - \alpha$ in the denominator. In view of $W_i^- = W_i^+(\zeta = 0)$, the growth rate of essentially super-critical particles, $di/dt =$

$W_i^+ - W_i^-$, equals to

$$\frac{di}{dt} = \frac{\zeta}{(1-\alpha)\tau} i^\alpha = \frac{m\zeta}{\tau} i^{(m-1)/m}. \quad (1.116)$$

The invariant size introduced in Table 1.2 is defined as follows: ρ is an i -dependent variable such that the regular growth rate of super-critical nuclei in terms of ρ is ρ -independent. As discussed in detail in Chap. 2, this variable is of paramount importance for the analytical description of different growth stages [3, 10, 17, 50–52]. For now, we just note that, due to $d\rho/dt = (d\rho/di)(di/dt)$, the invariant size is given by

$$\rho = i^{1-\alpha} = i^{1/m}, \alpha < 1; \quad \rho = \ln i, \alpha = 1. \quad (1.117)$$

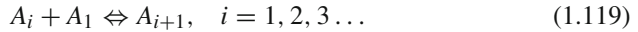
These relationships with different growth indices are also presented in Table 1.2. It is seen that the invariant size equals the particle radius (measured in the units of interatomic distance) in systems no. 2 and 7. In terms of growth indices, 3D surface islands growing in the ballistic regime from a 2D system appear to be equivalent to 3D droplets consuming a 3D vapor in the diffusion regime. Using (1.116), the growth rate in terms of the invariant size takes the form

$$\frac{d\rho}{dt} = \frac{\zeta}{\tau}, \quad (1.118)$$

thus being proportional to the supersaturation with a certain kinetic time constant τ .

1.8 Rate Equations of Nucleation Theory

Classical nucleation theory is based on the discrete set of rate equations for the time-dependent concentrations n_i of nuclei containing i monomers [7–9, 27, 50–52, 72–74]. In the case of homogeneous nucleation, we consider the monomolecular condensation and evaporation processes



where A_i denotes the nucleus with i monomers and A_1 is the free monomer of a metastable phase. It is assumed that the probability of collision between two nuclei is negligible, as well as many-body interactions. This essential property is normally ensured by a low concentration of nuclei (in vapors) or their disability to move (in surface systems). As above, the rate constants for the direct and reversed process (1.119) are denoted as W_i^+ and W_{i+1}^- , respectively. The entire reaction chain is illustrated in Fig. 1.24a. For a given “level” $i \geq 2$, the concentration of nuclei containing i monomers increases due to the condensation on the nuclei with $i - 1$ monomers and by the evaporation from the nuclei containing $i + 1$ monomers, and decreases

due to the condensation–evaporation processes on the nuclei with i monomers. The concentration of vapor changes in any of these condensation–evaporation processes. Production of dimer requires two monomers, while the decay of dimer creates two monomers. In most cases, the nucleation takes place under the dynamical conditions, where the total concentration of monomers can change in time, for example, due to a material influx into the system or desorption [3, 17, 50–52, 56]. To describe these processes, we introduce positive (“pumping”) and negative (“sink”) sources of monomers, denoted as P and $-Qn_1$, respectively. From balance considerations, the “quasi-chemical” set of rate equations for the concentrations $n_i(t) = [A_i]_t$ can be written down as

$$\frac{dn_1}{dt} = -2J_2 - \sum_{i=3}^{\infty} J_i + P - Qn_1 \quad (1.120)$$

$$\frac{dn_i}{dt} = J_i - J_{i+1}, \quad i = 2, 3, 4 \dots; \quad (1.121)$$

$$J_i = W_{i-1}^+ n_{i-1} - W_i^- n_i, \quad i = 2, 3, 4 \dots \quad (1.122)$$

Obviously, J_i is the flux of monomers from the level $i - 1$ to i . The condensation rate constants W_i^+ are always proportional to the monomer concentration n_1 : $W_i^+ = n_1 k_i^+$, with k_i^+ independent of n_1 .

From (1.120) and (1.121), it is easily seen that the total number of monomers in vapor and nuclei is changed in time only by pumping:

$$\frac{dn_1}{dt} + \frac{d}{dt} \sum_{i=2}^{\infty} in_i = P - Qn_1, \quad (1.123)$$

and remains constant at zero sources. Integration leads to the integral equation of material balance

$$n_{tot}(t) - n_{1e} = \int_0^t dt' [P(t') - Q(t')n_1(t')] = n_1(t) - n_{1e} + \sum_{i=2}^{\infty} in_i(t). \quad (1.124)$$

Here, the moment $t = 0$ corresponds to the equilibrium monomer concentration and, therefore, to zero n_i for all $i \geq 2$. Dividing (1.124) to n_{1e} , the material balance takes the non-dimensional form

$$\Phi(t) = \zeta(t) + G(t). \quad (1.125)$$

The left hand side is the so-called “ideal supersaturation” [10, 17, 50–52] that would be reached in the system without nucleation: $\Phi(t) = n_{tot}(t)/n_{1e} - 1$. Its time dependence is entirely determined by the external fluxes. The right hand side is the sum of the actual vapor supersaturation at time t and the total number of monomers in the

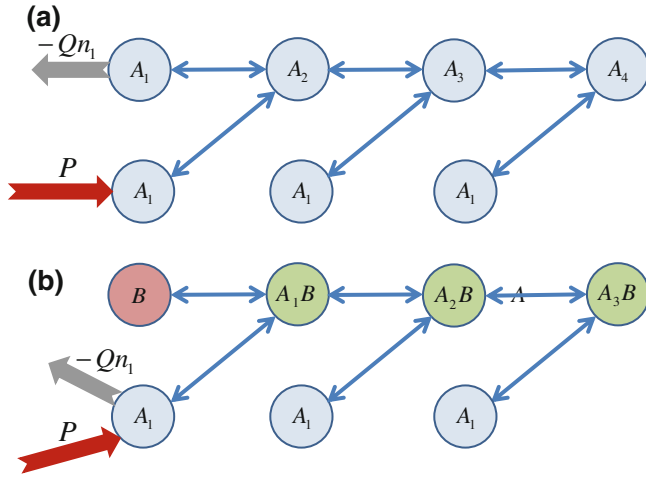
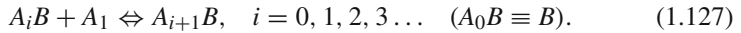


Fig. 1.24 Monomolecular reaction schemes for homogeneous (a) and heterogeneous (b) nucleation

condensed phase per unit volume, normalized to the equilibrium vapor concentration

$$G(t) = \frac{1}{n_{1e}} \sum_{i=2}^{\infty} i n_i(t). \quad (1.126)$$

The most common monomolecular reaction scheme describing heterogeneous nucleation [10, 73, 74] writes down as



Here, B denotes the condensation center or seed, for example, a charged ion in the gas-vapor system or a catalyst particle on the substrate surface; A_1 is the monomer and $A_i B$ with $i = 1, 2, 3 \dots$ are the heterogeneous clusters consisting of i monomers and one seed. Similarly to the previous case, the reaction chain is schematized in Fig. 1.24b. The set of kinetic equations for the concentrations of monomers $n_A(t) = [A_1]_t$ and clusters $n_i(t) = [A_i B]_t$ (at $i = 0$, $n_0(t) = [B]_t$ is the concentration of free seeds) is given by

$$\frac{dn_A}{dt} = - \sum_{i=1}^{\infty} J_i + P - Q n_A; \quad (1.128)$$

$$\frac{dn_i}{dt} = J_i (1 - \delta_{i0}) - J_{i+1}, \quad i = 0, 1, 2, 3 \dots; \quad (1.129)$$

$$J_i = W_{i-1}^+ n_{i-1} - W_i^- n_i, \quad i = 1, 2, 3 \dots \quad (1.130)$$

As above, P and Q describe the positive and negative sources of monomers. Kroneker's symbol δ_{io} in (1.29) disables the decay of condensation seed B . The flux given by (1.130) has the same form as in (1.122), however, the heterogeneous rate constants might be different, particularly for smaller clusters. The condensation rates W_i^+ are proportional to the monomer concentration n_A : $W_i^+ = n_A k_i^+$, with k_i^+ independent of n_A .

Summing up (1.129) with different i , it is seen that the total concentration of heterogeneous clusters (including the free nucleation centers) is preserved in time, because it equals the total number of available seeds per unit volume at any time. This is the main difference from the homogeneous case, where the total number of nuclei is not conserved. Similarly to (1.123), the total number of the monomers in vapor and nuclei is changed in time only by external sources. Therefore, (1.128) and (1.129) yield two conservation laws

$$\sum_{i=0}^{\infty} n_i = n_B^{tot}; \quad \frac{dn_A}{dt} + \frac{d}{dt} \sum_{i=1}^{\infty} i n_i = P - Q n_A, \quad (1.131)$$

where n_B^{tot} is the total concentration of nucleation centers.

All fluxes must cancel in the quasi-equilibrium state at a given vapor concentration n_1 , leading to the detailed balance

$$W_{i-1}^+ n_{i-1}^{eq} = W_i^- n_i^{eq}. \quad (1.132)$$

Here, the index i runs from 3 to infinity and from 2 to infinity in the homogeneous and heterogeneous cases, respectively. At $i = 2$, the principle of detailed balance yields $W_1^+ n_1 = W_2^- n_2^{eq}$ in the homogeneous case and $W_0^+ n_B = W_1^- n_1^{eq}$ in the heterogeneous case. Clearly, (1.132) also apply in the global equilibrium, where $n_1 = n_1^{eq}$ or $n_B = n_B^{eq}$ and i runs from 2 or 1. The quasi-equilibrium distribution (in the homogeneous case) can be presented in the form

$$n_i^{eq} = \prod_{k=2}^i (W_{k-1}^+ / W_k^-) n_1. \quad (1.133)$$

Comparing it to (1.70), we obtain the relationship between the formation energy and the ratios of evaporation–condensation rate constants:

$$F_i = \sum_{k=2}^i \ln (W_k^- / W_{k-1}^+). \quad (1.134)$$

Since the evaporation rates depend on many complex processes inside the nuclei and their independent determination is rather obscure, (1.132) is normally used the other way round. Indeed, while the W_i^- are generally unknown, the W_i^+ can be obtained by considering the mass transport into the particle, as demonstrated in

Sect. 1.8. The macroscopic formation energy is also well known, as discussed in Sect. 1.6. Hence, the principle of detailed balance enables the determination of the unknown evaporation rates by

$$W_i^- = W_{i-1}^+ \exp(F_i - F_{i-1}), \quad (1.135)$$

where F_i is given by (1.65) at $i \gg 1$.

In practice, the macroscopic description of nucleation process applies beginning from $i = i_c - \Delta i_c$, where i_c is the number of monomers in the critical nucleus and Δi_c is the half-width of the near-critical region, the quantities defined in Sect. 1.6. As shown in Sect. 1.8, the W_i^+ is a power law function of i , so that the W_{i-1}^+ in (1.135) can be changed to W_i^+ with a negligible relative error of $1/i$. As for the exponential term, the small parameter of the Taylor expansion

$$F_i - F_{i-1} = \frac{dF(i)}{di} - \frac{1}{2} \frac{d^2F(i)}{di^2} + \dots, \quad (1.136)$$

actually equals $1/\Delta i_c$ in the near-critical region $i_c - \Delta i_c < i < i_c + \Delta i_c$, where the relative error of neglecting the higher order terms is the largest. It is also clear that the relative error of substituting the integer i to real i in $\exp(-F_i)$ and, therefore, in quasi-equilibrium distribution, is smaller than $1/\Delta i_c$. Hence, (1.135) can be reduced to

$$W^-(i) = W^+(i) \exp[dF/di] \quad (1.137)$$

with small relative error in the range of interest at $1/\Delta i_c \ll 1$. The parameter $1/\Delta i_c$ is one of the two small parameters of classical nucleation theory, as discussed later on.

Further, using (1.132) in (1.130), we obtain a very useful representation for the flux:

$$J_i = W_{i-1}^+ n_{i-1}^{eq} (\tilde{n}_{i-1} - \tilde{n}_i). \quad (1.138)$$

Here, $\tilde{n}_i = n_i/n_i^{eq}$ is the concentration of nuclei of a given size, normalized to the corresponding quasi-equilibrium concentration.

1.9 Exact Solutions

Let us now consider the unique cases where the discrete set of rate equations can be solved exactly [50]. Although restricted to the specific choice of rate constants, these solutions are relevant for the foregoing analysis of real size spectra. With neglect of non-linearity caused by the time dependence of monomer concentration and in absence of evaporation, (1.129) can be simplified to

$$dp_0/dt = -p_0;$$

$$dp_i/dt = i^\alpha p_{i-1} - (i+1)^\alpha p_i, \quad i = 1, 2, 3 \dots \quad (1.139)$$

Here, $p_i(t)$ are the normalized ($\sum_{i=0}^{\infty} p_i(t) = 1$) probabilities $p_i(t)$ to find a particle with i monomers at time t . The normalized time t is now measured in the units of the characteristic time of particle growth. The growth rates di/dt of differently sized particles equal i^α with the exponent α ranging between 0 and 1, as discussed in Sect. 1.7. The model given by (1.139) can be called the linear irreversible growth at a constant supersaturation. The initial condition

$$p_i(t=0) = \delta_{i0} \quad (1.140)$$

means that all particles at $t = 0$ are concentrated at state $i = 0$ with zero size and probability $p_0(t=0) = 1$. In other words, we are searching for the solution for the Green function describing the time evolution of the initial delta-like package. Clearly, the time-dependent mean number of atoms in the nuclei (the mean size for brevity), $i_*(t)$, and the dispersion, $\psi(t)$, are given by

$$i_*(t) = \sum_{i=0}^{\infty} i p_i(t); \quad \psi(t) = \sum_{i=0}^{\infty} [i - i_*(t)]^2 p_i(t). \quad (1.141)$$

We now note that the discrete system of (1.139) has the unique exact solutions at integer $\alpha = 0$ and $\alpha = 1$, obtained in [74] (in a more general case) and containing some of earlier results by Montroll and Shuler [75], Rankin and Light [76] and Glauber [77] as the particular cases. The solutions to (1.139) with the initial condition (1.140) at $\alpha = 0$ are given by the Poisson distribution:

$$p_i(t) = e^{-t} \frac{t^i}{i!}. \quad (1.142)$$

This can be easily proved by the direct insertion of (1.142) into (1.139) at $\alpha = 0$, while meeting the initial condition is evident. For this distribution, $i_* = \psi = t$. At large t (and i), the Poisson spectrum asymptotically tends to the Gaussian

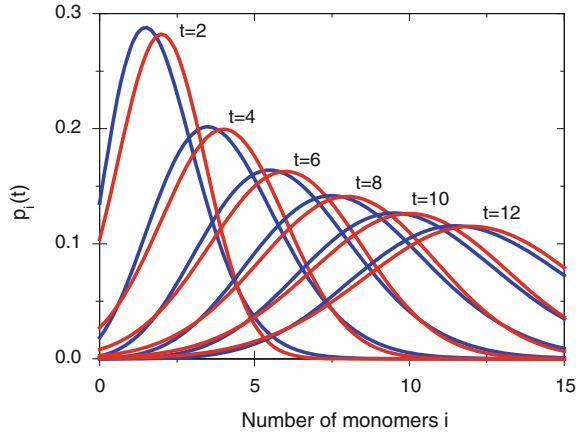
$$p(i, t) = \frac{1}{\sqrt{2\pi t}} \exp \left[-\frac{(i-t)^2}{2t} \right], \quad (1.143)$$

the property seen directly by applying the Stirling formula $i! \cong \sqrt{2\pi i} (i/e)^i$ to (1.142) at large i .

The second order continuum approximation of (1.139) at $\alpha = 0$ is obtained simply by the Taylor expansion of their right hand side at large i :

$$p_{i-1} - p_i = \left[\exp \left(-\frac{\partial}{\partial i} \right) - 1 \right] p_i \cong -\frac{\partial p(i, t)}{\partial i} + \frac{1}{2} \frac{\partial^2 p(i, t)}{\partial i^2}. \quad (1.144)$$

Fig. 1.25 Comparison between the Poisson (*blue curves*) and Gaussian (*red curves*) distributions at different t . Continuum Poisson spectra are guide for the eye only, since the Poisson distribution is defined only for integer i



The resulting Fokker-Plank type kinetic equation for the continuum size spectrum has the form

$$\frac{\partial p(i, t)}{\partial t} = -\frac{\partial p(i, t)}{\partial i} + \frac{1}{2} \frac{\partial^2 p(i, t)}{\partial i^2};$$

$$p(i, t = 0) = \delta(i). \quad (1.145)$$

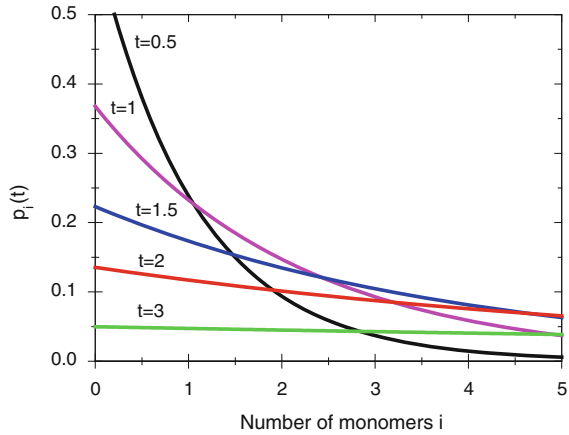
It is noteworthy that the diffusion-like spreading Gaussian given by (1.143) is the exact solution to the continuum (1.145). This is indeed the natural and well-known result for the diffusion-induced broadening of a delta-like package. Therefore, the discrepancy between the Poisson and Gaussian distributions originates as the difference in the exact solutions to the discrete set of kinetic equations and its continuum form. This difference rapidly becomes negligible toward larger i , as demonstrated in Fig. 1.25.

Very importantly, the system of (1.139) at $\alpha = 0$ describes exactly the low temperature growth of vapor-deposited thin film shown in Fig. 1.20, where the desorption and surface diffusion are negligible. The growth on the similar surface in homoepitaxy proceeds at the rate $V = \chi \sigma I$ (in monolayers per second (ML/s)). All layers $i = 0, 1, 2 \dots$ are identical. Such a growth leads to the Poissonian surface with the probabilities to find a random point of surface relief at the height $h = i$ MLs given by

$$p_i(t) = \exp[-\bar{h}(t)] \frac{\bar{h}^i(t)}{i!} \cong \frac{1}{\sqrt{2\pi\bar{h}(t)}} \exp\left[-\frac{(i - \bar{h}(t))^2}{2\bar{h}(t)}\right]. \quad (1.146)$$

The mean film thickness $\bar{h}(t) = \psi(t) = Vt$ equals the squared surface roughness. The last (1.146) applies for thick enough film with $\bar{h} \gg 1$.

Fig. 1.26 Time evolution of geometrical distribution



Exact solutions to the discrete set of (1.139) at $\alpha = 1$ with the initial condition (1.140) are given by the geometrical distribution

$$p_i(t) = \frac{1}{[i_*(t) + 1]} \left[\frac{i_*(t)}{i_*(t) + 1} \right]^i, \quad (1.147)$$

with the time-dependent mean size $i_*(t) = \exp(t) - 1$. The dispersion of the geometrical distribution is given by $\psi = i_*(1 + i_*)$. This distribution is much wider than the Poisson spectrum or the spreading Gaussian with the same mean size. Time evolution of this distribution, presented in Fig. 1.26, is distinctly different from the previous case at $\alpha = 0$. The Poissonian spectra are almost symmetrical and are well centered near the most representative size, whereas the geometrical distribution reaches its maximum at zero size at any time. In terms of variable i , the spectra shown in Fig. 1.26 do not feature any propagation of the most representative size toward larger i , but rather rapidly become flat already at $t = 3$.

Neglect of evaporation and the time dependence of monomer concentration is not essential for obtaining the exact solutions to the growth equations. The critical assumption regards the form of kinetic rate constants. The exact solution can be obtained in a simple analytical form when the rate constants are linear in i [74]. Let us show this in the case of heterogeneous nucleation described by (1.128–1.130). In the following, it is convenient to consider the normalized size distribution $f_i(t) = n_i(t)/n_B^{tot}$, and the normalized monomer concentration $f_A(t) = n_A(t)/n_B^{tot}$. As discussed, the condensation rate constants are proportional to the monomer concentration and can be put in the form $W_i^+ = f_A(t)k_i^+$, where k_i^+ is time-independent. Changing the notation of W_i^- to k_i^- , (1.128–1.130) take the form

$$\frac{df_A}{dt} = - \sum_{i=1}^{\infty} J_i + P - Qf_A; \quad (1.148)$$

$$\frac{df_i}{dt} = J_i(1 - \delta_{i0}) - J_{i+1}, \quad i = 0, 1, 2, 3 \dots; \quad (1.149)$$

$$J_i = k_{i-1}^+ f_A f_{i-1} - k_i^- f_i; \quad (1.150)$$

$$f_i(t=0) = \delta_{i0}; \quad f_A(t=0) = M(0), \quad (1.151)$$

with the obvious re-normalization of influx P . The quantity $M(0) = n_A^{tot}(0)/n_B^{tot}$ is the ratio of the total number of monomers to the number of available condensation seeds at $t = 0$. The two conservation laws for this system are given by

$$\sum_{i=0}^{\infty} f_i(t) = 1; \quad \frac{di_*}{dt} + \frac{df_A}{dt} = P - Qf_A(t), \quad (1.152)$$

where $i_*(t) = \sum_{i=0}^{\infty} i f_i(t)$ is the mean size of clusters.

We now consider the case of i -linear rate constants

$$k_i^+ = k^+(1 + \delta i); \quad k_i^- = k^- i, \quad (1.153)$$

where δ is an arbitrary positive constant. Since the direct integration of kinetic equations is much less obvious than in the previous cases, we introduce the generating function for probabilities $f_i(t)$ by definition

$$f(z, t) = \sum_{i=0}^{\infty} f_i(t) z^i. \quad (1.154)$$

Obviously, $f_i(t)$ are obtained as the coefficients of Taylor expansion for $f(z, t)$ at $z = 0$. From its definition, the generating function features the following important properties:

$$f(1, t) = 1; \quad \left. \frac{\partial f(z, t)}{\partial z} \right|_{z=1} = i_*(t). \quad (1.155)$$

Differentiating $f(z, t)$ with respect to time and using (1.149) and (1.150) leads to the following equation in the general case

$$\frac{\partial f(z, t)}{\partial t} = (z - 1)f_A(t) \sum_{i=0}^{\infty} k_i^+ f_i(t) z^i + \left(\frac{1}{z} - 1 \right) \sum_{i=1}^{\infty} k_i^- f_i(t) z^i. \quad (1.156)$$

This is useful only if the right hand side can be expressed through $f(z, t)$ and its derivatives with respect to z , resulting in the closed equation in partial derivatives for $f(z, t)$. This is exactly what happens when the rate constants are given by (1.153). In this case, (1.156) is reduced to the first order partial differential equation of the form

$$\frac{\partial f(z, t)}{\partial t} + (z - 1) [k^- - \delta k^+ f_A(t) z] \frac{\partial f(z, t)}{\partial z} = (z - 1) k^+ f_A(t) f(z, t). \quad (1.157)$$

Differentiating this with respect to z and putting $z = 1$, we get the differential equation for the mean size. Together with the second (1.152), it forms the closed system for the determination of $f_A(t)$ and $i_*(t)$ at given monomer sources:

$$\begin{aligned} \frac{di_*(t)}{dt} + [k^- - \delta k^+ f_A(t)] i_*(t) &= k^+ f_A(t); \\ \frac{df_A(t)}{dt} + \frac{df_A(t)}{dt} &= P(t) - Q(t) f_A(t); \\ f_A(t = 0) &= M(0); \quad i_*(t = 0) = 0. \end{aligned} \quad (1.158)$$

Solution to (1.157) can be found in analytical form, because one of its first integrals is obtained from the special type of integrable Riccati equation having the partial solution $z = 1$ [74]. In the case of mono-dispersive initial condition $f(z, t = 0) = 1$, the solution is given by

$$f(z, t) = [1 + \delta i_*(t)(z - 1)]^{-1/\delta}. \quad (1.159)$$

More generally, this solution holds whenever the initial condition to (1.157) has the form (1.159) with arbitrary mean size $i_*(0)$ at $t = 0$.

The Taylor expansion of the generating function given by (1.159) near $z = 0$ produces the Polya distribution of probabilities $f_i(t)$:

$$f_i(t) = [1 + \delta i_*(t)]^{-1/\delta} \frac{(1 + \delta)(1 + 2\delta) \dots (1 + (i - 1)\delta)}{i!} \left[\frac{i_*(t)}{1 + \delta i_*(t)} \right]^i. \quad (1.160)$$

We thus have proved the following theorem:

If the initial conditions to the discrete set of kinetic (1.148–1.150) with the size-linear rate constants (1.153) are given by the Polya distribution with arbitrary mean size $i_*(0)$, its form remains time-invariant during growth with only the mean size changing in time, the mono-dispersive initial distribution with $i_*(0) = 0$ being the particular case.

This interesting property is called the canonical invariance of the Polya distribution of probabilities. At $\delta = 1$, (1.160) is reduced to the geometrical distribution given by (1.147). At $\delta \rightarrow 0$, it is transformed to the Poisson distribution (1.142), where t is changed to $i_*(t)$. The dispersion of the Polya distribution is related to the mean size as

$$\psi(t) = i_*(t)[1 + \delta i_*(t)]. \quad (1.161)$$

The previous results therefore follow from (1.160) and (1.161) in the limit cases.

The time evolution of the mean size is primarily determined by the monomer fluxes. In particular, as follows from the second (1.158), the equilibrium monomer concentration at $t \rightarrow \infty$ is given by

$$f_A^{eq} = f_A(\infty) = P(\infty)/Q(\infty), \quad (1.162)$$

provided that the quantity in the right hand side remains finite at large t . From the first (1.158), we get the large time asymptote of the mean size

$$i_*(\infty) = \frac{k^+ f_A(\infty)}{k^- - \delta k^+ f_A(\infty)}. \quad (1.163)$$

This value is finite at $P(\infty)/Q(\infty) < k^-/\delta k^+$, the inequality giving the condition for the existence of the asymptotic equilibrium state with a finite mean size. Otherwise, the mean size increases infinitely at $t \rightarrow \infty$ and the global equilibrium is never reached. In the former case at a finite $i_*(\infty)$, the equilibrium Polya size distribution obeys the principle of detailed balance

$$k^+[1 + \delta(i-1)]f_A(\infty)f_{i-1}(\infty) = k^-if_i(\infty). \quad (1.164)$$

Interestingly, this equation shows that the equilibrium Polya distribution will be established at $t \rightarrow \infty$ for a more general system with the rate constants $k_i^+ = k^+(1 + \delta i)Y(i)$, $k_i^- = k^-iY(i-1)$. Here, $Y(i)$ is an arbitrary function of i that cancels in (1.164).

The system of (1.158) can be integrated exactly in some particular cases. For example, in the isolated system with $P = Q = 0$, the total number of monomers is conserved in time: $f_A(t) + i_*(t) = M = \text{const}$. The time evolution of the mean size is then determined by the non-linear equation

$$\frac{di_*(t)}{dt} = -\delta k^+ i_*^2(t) + (\delta k^+ M - k^+ - k^-)i_*(t) + k^+ M. \quad (1.165)$$

Solution to (1.165) with an arbitrary initial $i_*(0)$ has the form

$$i_*(t) = \frac{a_1 + |a_2| \exp[-\delta k^+(a_1 + |a_2|)t]}{1 - C \exp[-\delta k^+(a_1 + |a_2|)t]} \quad (1.166)$$

with

$$a_{1,2} = \frac{1}{2} \left(M - \frac{k^+ + k^-}{\delta k^+} \right) \pm \frac{1}{2} \left[\left(M - \frac{k^+ + k^-}{\delta k^+} \right)^2 + \frac{4M}{\delta} \right]^{1/2};$$

$$C = 1 - \frac{a_1 + |a_2|}{i_*(0)}. \quad (1.167)$$

It is seen that the mean size tends to its equilibrium value a_1 at $t \rightarrow \infty$, while the monomer concentration tends to $M - a_1$. At $\delta = 0$, (1.165) becomes linear in $i_*(t)$, with the corresponding solutions given by

$$\begin{aligned}
f_A(t) &= c^+ M + [f_A(0) - c^- M] \exp[-(k^+ + k^-)t]; \\
i_*(t) &= c^- M - [f_A(0) - c^- M] \exp[-(k^+ + k^-)t].
\end{aligned} \tag{1.168}$$

Here, $c^\pm = k^\pm / (k^+ + k^-)$ are the relative values of the condensation and evaporation rate constants. Obviously, the mean size and the monomer concentration tend to $c^+ M$ and $c^- M$, respectively, regardless of the initial conditions.

Finally, the solutions to the linear system of (1.158) at $\delta = 0$ with the time-independent monomer sources $P = \text{const}$, $Q = \text{const}$ and arbitrary initial conditions can be obtained in the form

$$\begin{aligned}
f_A(t) &= \frac{P}{Q} + C_1 \exp(-\omega_1 t) + C_2 \exp(-\omega_2 t); \\
i_*(t) &= \frac{k^+ P}{k^- Q} + \left(\frac{\omega_2}{k^-} - 1\right) C_1 \exp(-\omega_1 t) + \left(\frac{\omega_1}{k^-} - 1\right) C_2 \exp(-\omega_2 t).
\end{aligned} \tag{1.169}$$

The constants are determined by

$$\begin{aligned}
\omega_{1,2} &= \frac{1}{2} (k^+ + k^- + Q) \mp \frac{1}{2} \left[(k^+ + k^- + Q)^2 - 4k^- Q \right]^{1/2}; \\
C_1 &= M(0) - \frac{\omega_2 [f_A(0) + P/Q] - P - k^- M(0)}{\omega_2 - \omega_1}; \\
C_2 &= \frac{\omega_2 f_A(0) + \omega_1 P/Q - P - k^- M(0)}{\omega_2 - \omega_1}.
\end{aligned} \tag{1.170}$$

Obviously, $\omega_2 > \omega_1 > 0$, yielding the asymptotic equilibrium values $f_A(\infty) = P/Q$ and $i_*(\infty) = (k^+ P)/(k^- Q)$, which is consistent with (1.162) and (1.163) at $\delta = 0$.

To summarize the results of this section, the exact solutions to the discrete kinetic equations of nucleation theory can be obtained in the case of i -linear condensation-evaporation constants. The size spectrum in terms of i variable features a remarkable time invariance of the Polya distribution. The form of this distribution is preserved in time, and depends on time only through the mean size of particles. At $\delta = 0$, the Polya spectrum takes the Poissonian form, which is rapidly converted to the Gaussian as the particles grow. At $\delta = 1$, it is reduced to the geometrical distribution. The dispersion of size spectrum increases with δ , featuring the linear dependence on the mean size at $\delta = 0$ and the quadratic dependence $i_*(1 + \delta i_*)$ at $\delta > 0$. The distribution shape also changes drastically with increasing δ . While the Poissonian and Gaussian spectra are centered near the most representative size (which is very close to the mean size for the Poisson distribution and equals the mean size for the symmetrical Gaussian), the geometrical distribution is essentially asymmetric. Its most representative size equals zero at any time, so that the spectrum rapidly flattens in terms of i variable as the particles grow.

The exact solutions presented here can be very useful in analyzing the model systems such as the low temperature thin films, vapor clusters in supersonic free jet expansions, population dynamics and many others, as well as for checking the validity of various approximate analytical methods, as discussed later on. They can describe quite well the irreversible growth at high enough supersaturations. However, the model (1.153) have one major difference from most real systems, whose typical feature is the maximum of formation energy at the critical size, the situation shown in Fig. 1.13. Indeed, since the condensation constant is positive and the evaporation constant starts from zero at $i = 0$, the curves k_i^+ and k_i^- can either never meet or intercept at a certain point i_0 such that $k_i^+ > k_i^-$ at $i < i_0$ and $k_i^+ < k_i^-$ at $i > i_0$. The condition $k_i^+ > k_i^-$ at any i corresponds to the irreversible growth, as described above. The interception case relates to the stable nucleus with i_0 monomers, since smaller particles tend to grow and larger particles tend to evaporate. This is exactly opposite to the critical size of nucleation theory i_c , which is in unstable equilibrium with a supersaturated environment. This yields the thermodynamically preferred evaporation at $i < i_c$ and growth at $i > i_c$. Therefore, the linear model for the rate constants cannot adequately describe the nucleation instability where the particles surpass the nucleation barrier due to thermodynamic fluctuations and start growing irreversibly only after entering the super-critical region.

1.10 Continuum Approximation

In the vast majority of applications, we deal with large enough nucleus consisting of many monomers. The continuum approximation at $i \gg 1$ [3, 7–19, 22–25, 50–52] converts the infinite set of ordinary differential equations to just one second order partial differential equation, which is clearly of great help for theoretical analysis. Let us write down the discrete kinetic (1.121) and (1.122) in the form

$$\frac{dn_i}{dt} = W_{i-1}^+ n_{i-1} + W_{i+1}^- n_{i+1} - (W_i^+ + W_i^-) n_i. \quad (1.171)$$

Continuum approximation is obtained simply by the Taylor expansion of the non-diagonal terms in the right hand side around i and leaving only the first and the second order derivatives with respect to i :

$$\begin{aligned} W_{i-1}^+ n_{i-1} &\cong W_i^+ n_i - \frac{\partial}{\partial i} (W_i^+ n_i) + \frac{1}{2} \frac{\partial^2}{\partial i^2} (W_i^+ n_i); \\ W_{i+1}^- n_{i+1} &\cong W_i^- n_i + \frac{\partial}{\partial i} (W_i^- n_i) + \frac{1}{2} \frac{\partial^2}{\partial i^2} (W_i^- n_i). \end{aligned} \quad (1.172)$$

As discussed, the condensation rate is usually a power law function of i , while the evaporation rate is related to W_i^+ by (1.137). Hence, the differentiation of the rate constants gives the multiplying factor of the order of $1/i$ in the corresponding terms.

This factor is of the order of $1/i_c$ in the near-critical region. If n_i was the quasi-equilibrium distribution, its derivatives would decrease as $1/\Delta i_c$. The same factor appears upon differentiating the Gaussian with the half-width Δi_c . Therefore, the small parameter of the expansions given by (1.172) is $1/\Delta i_c$. The Taylor expansion of kinetic constants is $i_c/\Delta i_c$ times more accurate than that of n_i in typical cases.

Inserting (1.172) into (1.171) and introducing the continuum distribution function $n(i, t)$ that equals $n_i(t)$ in the discrete integer points, we arrive at the Fokker-Plank type kinetic equation of the form

$$\frac{\partial n(i, t)}{\partial t} = -\frac{\partial}{\partial i} \left[A(i)n(i, t) - B(i)\frac{\partial n(i, t)}{\partial i} \right]. \quad (1.173)$$

Kinetic coefficients at the first and second derivative with respect to size

$$\begin{aligned} A(i) &\equiv \frac{di}{dt} = W^+(i)[1 - \exp(dF(i)/di)]; \\ B(i) &= \frac{1}{2}W^+(i)[1 + \exp(dF(i)/di)] \end{aligned} \quad (1.174)$$

describe the regular growth rate and the kinetic fluctuations, respectively. Equation (1.173) with coefficients (1.174) is also called the Becker–Doering–Zeldovich equation. In the essentially super-critical region $i > (5 - 6)i_c$, where $dF(i)/di \cong -\ln(\zeta + 1)$, the kinetic coefficients are simplified to

$$\begin{aligned} A(i) &= \frac{W^+(i)\zeta}{\zeta + 1} = \frac{m\zeta}{\tau} i^{(m-1)/m}; \\ B(i) &= \frac{W^+(i)(\zeta + 2)}{2(\zeta + 1)} = \frac{m(\zeta + 2)}{2\tau} i^{(m-1)/m}. \end{aligned} \quad (1.175)$$

The last expressions in the right hand side apply when the condensation rate is given by the scaling (1.115). Equations (1.175) do not account for the interactions of the critical size with the spectrum and are not applicable either in the near-critical region or at the late Ostwald ripening stage. At $\Delta i_c/i_c \ll 1$ (this inequality will be discussed in more detail later on), the kinetic coefficients $A(i), B(i)$ in (1.173) can be taken out of derivatives, at least at the regular growth stage.

Continuum kinetic equation of nucleation theory (1.173) contains the unknown supersaturation entering its coefficients as given by (1.174). Therefore, it should be coupled with the integral equation of material balance. In the case of homogeneous nucleation, the corresponding (1.125) and (1.126) are re-written as

$$\Phi(t) = \zeta(t) + G(t); \quad G(t) = \frac{1}{n_{1e}} \int_0^\infty di n(i, t). \quad (1.176)$$

Here, as above, the function $G(t)$ represents the total number of monomers distributed in all nuclei. Equations (1.173) and (1.176) give the closed system of equations for finding $n(i, t)$ and $\zeta(t)$ at the known monomer sources.

1.11 Stationary State

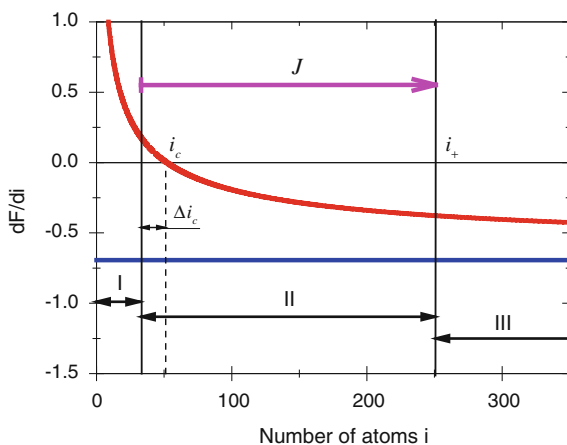
It has already been shown that classical nucleation theory applies when the nucleation barrier is high enough. In this case, we can divide the entire size axis into three regions with distinctly different behaviors, as shown in Fig. 1.27. Due to the smallness of fluctuations, the quasi-equilibrium state at a given supersaturation should be observed in the subcritical region $i \leq i_c - \Delta i_c$ [12]:

$$n_i = n_i^{eq}, \quad i \leq i_c - \Delta i_c. \quad (1.177)$$

The near-critical region $i_c - \Delta i_c < i < i_c + \Delta i_c$ is expected to quickly evolve to the stationary state n_i^s such that the particle flux through it is size-independent: $J_i = J^s \equiv J$. In fact, the stationary flux propagates even further toward $i_+ \sim (5-6)i_c$, the region where the curvature effects become negligible and the derivative of the formation energy with respect to i can be approximated by a constant (see Fig. 1.27). It is this stationary state that will be studied in detail in this section. In the essentially supercritical region $i > i_+$, the nuclei grow irreversibly at the rate given by the first (1.175). We underline that the stationary state relates to a particular supersaturation value and changes almost instantaneously with ζ . This important feature holds because the time needed to establish the stationary size distribution in near-critical region at a given ζ is much shorter than the macroscopic time required to change the supersaturation itself.

The stationary flux through the near-critical region gives the nucleation rate [3, 7–10, 17, 27], also called the Zeldovich nucleation rate [12], probably the most important characteristic of any nucleation process. At a given supersaturation, J equals the number of irreversibly growing nuclei emerging in the unit volume (or on the unit surface area) per unit time. These super-critical nuclei emerge due to thermodynamic fluctuations in the subcritical region, surpassing the nucleation barrier at the rate J .

Fig. 1.27 Schematic representation of the subcritical (the quasi-equilibrium) region I, the extended near-critical (the fluctuational) region II and the essentially supercritical (the growth) region III. The red line shows dF/di for 2D islands at $a = 10$ and $\zeta = 1$, the blue line is its supercritical asymptote. Stationary flux J through the near-critical region is the nucleation rate at a given supersaturation



Let us now see how the stationary distribution and the corresponding nucleation rate can be obtained in the frame of discrete theory. We consider (1.138) for the flux assuming that the stationary spectrum n_i^s tends to zero at large enough i , the property that should hold for any reasonable physical distribution. Summing up (1.138) with $J = \text{const}$ at $k = i, i + 1, i + 2 \dots$ beginning from $i \sim i_c - \Delta i_c$, we obtain

$$n_i^s = J n_i^{eq} \sum_{k=i}^{\infty} \frac{1}{W_k^+ n_k^{eq}}. \quad (1.178)$$

From (1.177), the condition $n_{i_c - \Delta i_c}^s = n_{i_c - \Delta i_c}^{eq}$ should be met at the boundary of near-critical and subcritical region. This can be ensured only by the specific choice of constant J in (1.178), given by [27]

$$J = \left(\sum_{k=i_c - \Delta i_c}^{\infty} \frac{1}{W_k^+ n_k^{eq}} \right)^{-1}. \quad (1.179)$$

As discussed already in Sect. 1.9, the equilibrium distribution at integer i can be substituted to the continuum function $n^{eq}(i)$ with the relative error $1/\Delta i_c \ll 1$. The sum in (1.179) can be then changed to the integral with the same accuracy, yielding

$$J = \left(\int_{i_c - \Delta i_c}^{\infty} \frac{di}{W^+(i) n^{eq}(i)} \right)^{-1}. \quad (1.180)$$

The continuum analogue of (1.178) for the stationary distribution is given by

$$n^s(i) = J n^{eq}(i) \int_i^{\infty} \frac{di'}{W^+(i') n^{eq}(i')}, \quad i \geq i_c - \Delta i_c. \quad (1.181)$$

Let us consider the integral in the right hand side of (1.180) for the nucleation rate. Due to a very sharp dependence of quasi-equilibrium distribution on i , the formation energy can be approximated by the parabolic dependence near the critical size i_c as

$$F(i) \cong F - \frac{(i - i_c)^2}{\Delta i_c^2}. \quad (1.182)$$

Inserting this into the exponent under the integral, transforming it to the variable $x = (i - i_c)/i_c$ and using the Laplace method for asymptotic calculation of integrals containing a large parameter in the exponent, we obtain

$$\int_{i_c - \Delta i_c}^{\infty} \frac{di}{W^+(i) n^{eq}(i)} = \frac{\exp(F)}{n_1} i_c \int_{-\Delta i_c/i_c}^{\infty} \frac{dx}{W^+(x)} \exp \left[- \left(\frac{i_c}{\Delta i_c} \right)^2 x^2 \right] \cong \frac{\exp(F)}{n_1} \frac{\Delta i_c}{W^+(i_c)} \sqrt{\pi}. \quad (1.183)$$

It is seen that the parameter $\Delta i_c/i_c$ should be much smaller than one to justify the final result.

Using this in (1.180), we arrive at the famous Zeldovich formula for the nucleation rate [3, 7–10, 12]

$$J = \frac{1}{\sqrt{\pi} \Delta i_c} n_1 W^+(i_c) \exp(-F). \quad (1.184)$$

The nucleation rate is thus proportional to the inverse exponent of the nucleation barrier at a given supersaturation, the condensation rate on the critical nucleus and the monomer concentration. The factor $1/\sqrt{\pi} \Delta i_c$ originating from the asymptotic integration is called the non-equilibrium Zeldovich factor. In view of $1/\Delta i_c \ll 1$, it is usually much smaller than one. Using the definition for the half-width of nucleation energy in the near-critical region, $\Delta i_c = \sqrt{2/|F''(i_c)|}$, (1.184) can be put in the equivalent form [3]

$$J = \sqrt{\frac{|F''(i_c)|}{2\pi}} n_1 W^+(i_c) \exp(-F). \quad (1.185)$$

As follows from the analysis of stationary state in the near-critical region, the two small parameters of macroscopic nucleation theory are given by [78]

$$1/\Delta i_c \ll 1; \quad \Delta i_c/i_c \ll 1. \quad (1.186)$$

The first strong inequality is required to justify the transformation from discrete to continuum distribution, while the second one is needed to use the Laplace method leading to the Zeldovich expression for the nucleation rate. Let us check the validity of these inequalities in some typical cases. For a 3D droplet or crystal nucleus in a 3D or 2D environment, Δi_c is given by (1.69) at $d = 3$, yielding

$$\Delta i_c = \frac{3}{\sqrt{a}} i_c^{2/3}; \quad \frac{\Delta i_c}{i_c} = \frac{3}{\sqrt{a} i_c^{1/3}}, \quad d = 3. \quad (1.187)$$

It is clear that the inequalities (1.186) are indeed valid at typical values of a of the order of ten and i_c of the order of several tens of monomers. For a 2D island, (1.69) gives

$$\Delta i_c = 2\sqrt{\frac{2}{a}} i_c^{3/4}; \quad \frac{\Delta i_c}{i_c} = 2\sqrt{\frac{2}{a}} \frac{1}{i_c^{1/4}}, \quad d = 2, \quad (1.188)$$

showing that the inequalities defined by (1.186) are again relevant at large enough a and i_c of the order of several tens. We note, however, that the first inequality (1.186) is always satisfied much better than the second one.

In the continuum theory, the size distribution obeys the Fokker-Plank-type (1.173), where the nucleus flux is defined as

$$J(i) = A(i)n(i) - B(i)\frac{\partial n(i)}{\partial i}. \quad (1.189)$$

In the near-critical region $i_c - \Delta i_c < i < i_c + \Delta i_c$ where dF/di is small, (1.174) are simplified to

$$A(i) \cong -W^+(i)dF/di; \quad B(i) \cong W^+(i) \quad (1.190)$$

with the accuracy $1/\Delta i_c$. Substitution of these expressions into (1.189) gives the stationary flux in the form

$$J = -W^+(i)n^{eq}(i)\frac{\partial \tilde{n}^s(i)}{\partial i}, \quad (1.191)$$

where \tilde{n}^s is the stationary distribution normalized to the equilibrium one. Obviously, the discrete (1.138) yields the same result for J at $\tilde{n}_{i-1} - \tilde{n}_i \cong -\partial \tilde{n}(i)/\partial i$, the approximation valid in the near-critical region with the adopted accuracy. Straightforward integration of (1.191) with the boundary conditions $n^s(i_c - \Delta i_c) = n^{eq}(i_c - \Delta i_c)$ and $n^s(i) \rightarrow 0$ at $i \rightarrow \infty$ yields exactly the same results for the nucleation rate and stationary distribution as those given by (1.180) and (1.181), respectively.

As for the stationary distribution, (1.178) can be considerably simplified when the particle size approaches the boundary of the near-critical and super-critical regions i_+ . At large enough $i \geq i_+$, the formation energy can be approximated by $F_i \cong -\ln(\zeta + 1)i$, therefore

$$n_i^s = J \sum_{k=i}^{\infty} \frac{1}{W_k^+} e^{F_k - F_i} \cong \frac{J}{W_i^+} \sum_{k=i}^{\infty} e^{-\ln(\zeta+1)(k-i)} = \frac{J}{W_i^+} \frac{(\zeta + 1)}{\zeta}. \quad (1.192)$$

Taking the rate constant out of summation is justified by its power law size dependence with the adopted accuracy. The end result is obtained simply by summation of the geometrical progression. Comparing the obtained expression to (1.115) and (1.116), it is seen that the stationary distribution in the essentially super-critical region has the “drift” form

$$n_i^s = \frac{J}{di/dt}. \quad (1.193)$$

This formula shows simply that, in the stationary state, the nuclei emerge at the rate J and surpass the boundary of the near-critical and super-critical regions with the speed di/dt . Of course, the latter should be treated as the nucleus growth rate without the curvature effects, as given by (1.116). For the power law dependence of the condensation rate constant as defined in (1.115), the stationary distribution takes the form

$$n_i^s = \frac{J\tau}{m\zeta i^{(m-1)/m}}, \quad (1.194)$$

where m is the growth index and τ is the characteristic growth time of super-critical nuclei. This expression is of major importance in the foregoing analysis, as it provides the boundary condition for the size distribution in the growth region. The same representation for $n^s(i)$ at $i \geq i_+$ can also be derived from the continuum (1.181).

Several works [10, 29, 79] have been studied how the stationary state is established in the near-critical region and what is the characteristic time t_s of this process in particular. The average estimate for t_s is given by

$$t_s \sim \frac{1}{|F''(i_c)| W^+(i_c)}. \quad (1.195)$$

This time is extremely short for most systems of interest. For example, it is not longer than 10^{-4} s in the case of 2D adatom condensation, which is evidently much shorter than the typical nucleation times. As mentioned already, the smallness of t_s on the time scale of interest justifies well the major assumption of a time-independent supersaturation while considering the stationary state. Since the latter is adjusted almost instantaneously to the current value of supersaturation, (1.184) and (1.194) can be treated as being parametrically time-dependent through $\zeta(t)$. The supersaturation is a “slow” variable at the stage considered. In the timescale hierarchy of the entire nucleation-condensation process, the initial step of establishing the stationary state in the near-critical region is the shortest.

Explicit representation for the nucleation rate as a function of supersaturation is obtained from the general (1.184) using (1.69) for Δi_c and (1.67) for $F(\zeta)$. We allow for the Kashchiev and Lothe-Pound modifications of nucleation barrier as defined by (1.71–1.73) and (1.74), respectively by writing the nucleation rate as $F(\zeta) + \Delta$. Here, $\Delta = -F_1 = -a + \ln(\zeta + 1)$ in the Kashchiev’s case and $\Delta = \ln(\sigma n_1) = \ln \theta_{1e} + \ln(\zeta + 1)$ in the Lothe-Pound case, with σ being the elementary volume in 3D case or surface area in 2D case, as discussed in Sect. 1.5. Obviously, the Δ -shift changes only the pre-exponent of the Zeldovich formula for the nucleation rate and does not affect either the ζ -dependence of the nucleation barrier or the coefficients of kinetic equation for the size distribution. After simple calculations, one obtains

$$J(\zeta) = \frac{n_{1e}}{\tau} \sqrt{\frac{a}{2\pi}} \frac{m\sqrt{d-1}}{d} (\zeta + 1)^2 \left[\frac{d \ln(\zeta + 1)}{(d-1)a} \right]^{(1-d)/2+d/m} \left(\frac{e^a}{\zeta + 1} \right)^\kappa \frac{1}{[\sigma n_{1e}(\zeta + 1)]^\vartheta} \\ \times \exp \left[-\frac{(d-1)^{d-1} a^d}{d^d \ln^{d-1}(\zeta + 1)} \right]. \quad (1.196)$$

Here, κ and ϑ equal one if the Kashchiev’s or the Lothe-Pound corrections are included and zero otherwise.

Let us consider some particular cases where (1.196) is reduced to the commonly used expressions. In their studies of 3D droplet condensation, Kuni *et al.* [10, 17] simply put $\Delta = 0$, the assumption used also in [14, 19, 53]. In the case of 3D droplets or islands growing in the ballistic regime ($d = m = 3$) with $\kappa = 0$ and $\vartheta = 0$, this

yields the nucleation rate in the form

$$J(\zeta) = \frac{n_{1e}}{\tau} \sqrt{\frac{a}{\pi}} (\zeta + 1)^2 \exp \left[-\frac{4a^3}{27 \ln^2(\zeta + 1)} \right]. \quad (1.197)$$

The corresponding stationary distribution written in terms of invariant size $\rho = i^{1/3}$ is given by

$$f_s(\zeta) = \frac{I(\zeta)}{d\rho/dt} = \frac{I(\zeta)\tau}{\zeta} = n_{1e} \sqrt{\frac{a}{\pi}} \frac{(\zeta + 1)^2}{\zeta} \exp \left[-\frac{4a^3}{27 \ln^2(\zeta + 1)} \right]. \quad (1.198)$$

When modified by the Kashchiev's re-normalization, the nucleation rate of 3D particles takes the form

$$J(\zeta) = \frac{n_{1e}}{\tau} \sqrt{\frac{a}{\pi}} e^a (\zeta + 1) \exp \left[-\frac{4a^3}{27 \ln^2(\zeta + 1)} \right]. \quad (1.199)$$

Similar expressions apply for liquid or solid 3D islands on a solid surface, with the corresponding modification of the surface energy constant a depending on the island shape.

In application to nucleation of vapor-deposited thin films, Kukushlin and Osipov [3] used the Lothe-Pound entropy correction. In the case of 2D surface islands growing in the ballistic regime ($d = m = 2$), $\kappa = 0$ and $\vartheta = 1$ (1.196) is reduced to the result of [3, 66]:

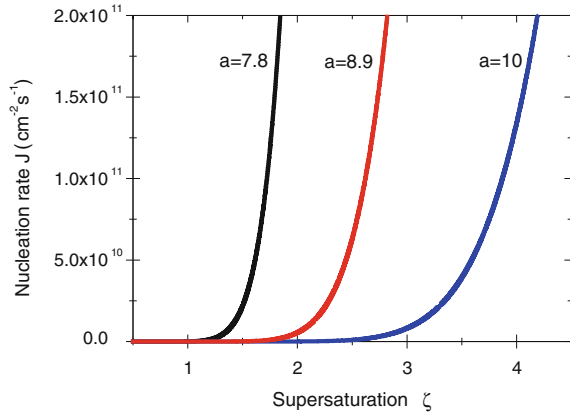
$$J(\zeta) = \frac{1}{\sqrt{\pi} \sigma \tau} (\zeta + 1) \ln^{1/2}(\zeta + 1) \exp \left[-\frac{a^2}{4 \ln(\zeta + 1)} \right]. \quad (1.200)$$

When the renormalization is of the Kashchiev's type, (1.200) is changed to

$$J(\zeta) = \frac{n_{1e}}{\sqrt{\pi} \tau} e^a (\zeta + 1) \ln^{1/2}(\zeta + 1) \exp \left[-\frac{a^2}{4 \ln(\zeta + 1)} \right]. \quad (1.201)$$

Very importantly, the Zeldovich expressions for the nucleation rate and stationary size distribution feature an extremely steep exponential dependence on supersaturation through $F(\zeta)$. This property follows directly from (1.73) for the nucleation barrier containing a large factor $a \gg 1$. The nucleation rate is so sensitive to supersaturation that a relatively small variation of the latter changes $J(\zeta)$ by the order of magnitude. The effect is demonstrated in Fig. 1.28, where the nucleation rate of 2D surface islands given by (1.200) is plotted against supersaturation at fixed $\sigma = 0.16 \text{ nm}^2$, $\tau = 3 \times 10^{-3} \text{ s}$ and different surface energy coefficients a . The threshold character of nucleation is clearly seen, with the threshold values of supersaturation increasing approximately from 1.4 to 3 with a changing from 7.8 to 10. When supersaturation exceeds the threshold value, the $J(\zeta)$ curve rapidly becomes

Fig. 1.28 Nucleation rate $J(\zeta)$ at three different a



almost vertical. At $a = 7.8$, the increase of supersaturation only from 1.7 to 1.8 results in ~ 4 times increase in the nucleation rate.

The Zeldovich formula for the nucleation rate has been verified experimentally in many material systems by measuring the number of emerging nuclei at different conditions such as the growth time, temperature, or material influx. At a known supersaturation, such measurements may be helpful in deducing important information about the surface energy for example. Indeed, writing (1.197) in the case of 3D surface islands in the simplified form

$$J = J_0 \exp \left[-\frac{b}{(k_B T)^3 \ln^2(\zeta + 1)} \right] \quad (1.202)$$

with $b = (4/27)a^3(k_B T)^3$ and assuming that the initial adatom concentration equals It_A , we obtain $\zeta + 1 = n_1/n_{1e} = I\tau_A/n_{1e}$. Using the temperature dependences $n_{1e} = n_0 \exp(-2T_c/T)$ and $\tau_A = \tau_A^0 \exp(E_A/k_B T)$, we arrive at

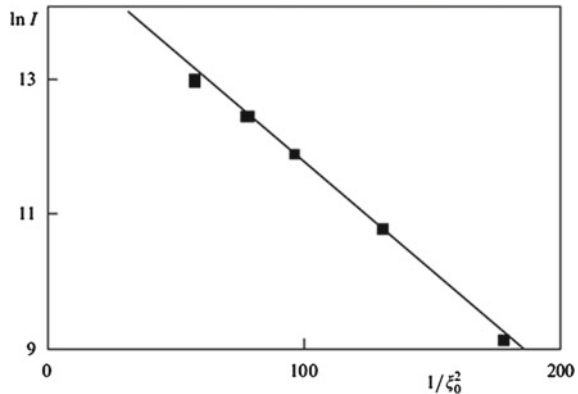
$$\ln \left(\frac{J}{J_0} \right) = -\frac{T_I}{T}; \quad T_I = \frac{b}{k_B [E_A + 2k_B T_c + k_B \tilde{T} \ln(I\tau_A^0/n_0)^2]}, \quad (1.203)$$

where \tilde{T} is the average temperature within the analyzed temperature range. Linear dependence of $\ln J$ on $1/T$ has been observed in many experiments with surface islands, the corresponding data can be found, for example, in [3]. Measuring the slope angle of the experimental curve enables finding the constant b and therefore the surface energy.

When plotted against supersaturation, (1.202) takes the form

$$\ln \left(\frac{J}{J_0} \right) = -\frac{b'}{\ln^2(\zeta + 1)} \cong -\frac{b'}{\zeta^2}, \quad (1.204)$$

Fig. 1.29 Experimental (symbols) and theoretical (line) dependences of the nucleation rate ($\text{m}^2 \text{s}^{-1}$) on the relative super-heating [3]



with $b' = (4/27)a^3$. The last expression applies when the supersaturation is much smaller than one. In this case, the nucleation process is slow and the emerging islands are large, which makes them easier to measure experimentally. Figure 1.29 shows the experimental dependence of $\ln J$ on $1/\zeta_0^2$ for the system of the lead zirconate–titanate ferroelectric islands, where ζ_0 is the relative super-heating (an analogue of initial supersaturation) [85]. It is seen that the experimental points are well fitted with the linear dependence following from the Zeldovich equation.

To summarize, at high enough nucleation barriers, the quasi-equilibrium state is thoroughly maintained in the subcritical region of sizes. The stationary state with the size-independent nucleus flux through the near-critical region is established very rapidly and pertains during the follow-up nucleation and growth stages by adjusting itself to the time-dependent supersaturation. The nucleation rate depends on the supersaturation primarily via the inverse exponent of nucleation barrier. This leads to an extremely high sensitivity of the entire nucleation process to the value of supersaturation. In the imperfect systems with chemical potential other than $\Delta\mu = k_B T \ln(\zeta + 1)$, all the results presented above remain valid upon substitution of $\Delta\mu/k_B T$ in the corresponding expressions. In particular, this applies to (1.184), (1.185), (1.196), (1.197), (1.199) to (1.201) for the nucleation rate and (1.193), (1.194), (1.198) for the stationary size distribution. However, the equation of state $\Delta\mu(\zeta)$ should be known for performing concrete calculations, while the unknown ζ must be obtained from the material balance condition in any case.

1.12 Stages of Nucleation-Condensation Process

This section presents a semi-quantitative preview of different stages of nucleation-condensation process, which will be considered in more detail in Chap. 2. As discussed, the shortest nucleation step is the establishment of stationary state in the near-critical region. The nucleation rate J depends on supersaturation, material con-

stants and temperature. In some scenarios of nanostructure formation, the Zeldovich formula for J alone provides a sufficient basis for modeling the entire growth process. Let us consider a very important case of nucleation in restricted nano-volumes or on nano-surfaces [45, 80–83]. Typical examples of such systems include a droplet of supersaturated liquid alloy (Fig. 1.30a), a vertical nanowire growing directly from vapor (Fig. 1.30b) or from a liquid alloy in the nanodroplet seated atop the nanowire (Fig. 1.30c). Provided that the available volume of a metastable phase or the surface area of the nanowire top facet is small enough, the nucleation will proceed in the so-called mononuclear mode [7]. In this mode, the characteristic time between two consecutive nucleation events is much longer than the time required for a nucleus to spread over the entire available volume or surface area. In the nanowire case, the vertical growth rate in the mononuclear mode is determined by the waiting time between the two nucleation events rather than by the lateral growth time of the island.

By its physical sense, the Zeldovich nucleation rate in the mononuclear mode gives the nucleation probability per unit time per unit volume. The total nucleation probability per unit time is therefore proportional to the available volume or surface area

$$V_{nuc}(\zeta, R) = I(\zeta, R)cR^d \quad (1.205)$$

with c as the corresponding shape constant, R as the linear size and $d = 3$ or 2 depending on the system dimension. The supersaturation value should be generally obtained by balancing the mass transport into the nanoparticle and the material sink caused by the nucleation. In some cases such as the steady state “vapor–liquid–solid” growth of nanowires [82], the supersaturation remains almost constant during the entire growth process due to a repeated material refill from vapor after each nucle-

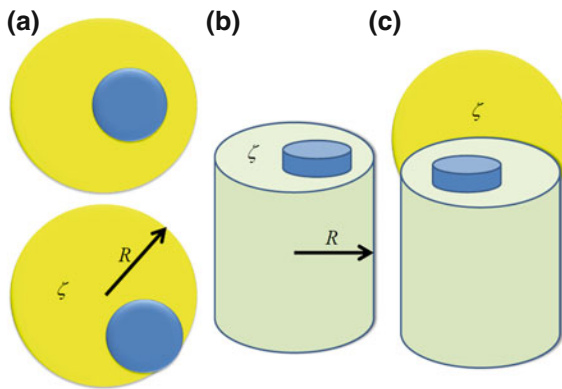


Fig. 1.30 Nucleation of islands in the volume of nanodroplet (a), on the top facet of self-induced nanowire (b) and of the vapor–liquid–solid nanowire (c) in the mononuclear mode. The nucleation rate is generally a function of supersaturation ζ in the droplet (a and c) or in the adatom system (b), and the radius R . a shows two different positions of the nucleus either entirely surrounded by the liquid or emerging partly at the liquid–vapor interface

ation event. Such a growth can be considered as the re-iterative, nucleation-mediated building of nanowire monolayers under the droplet, which proceeds under exactly identical conditions.

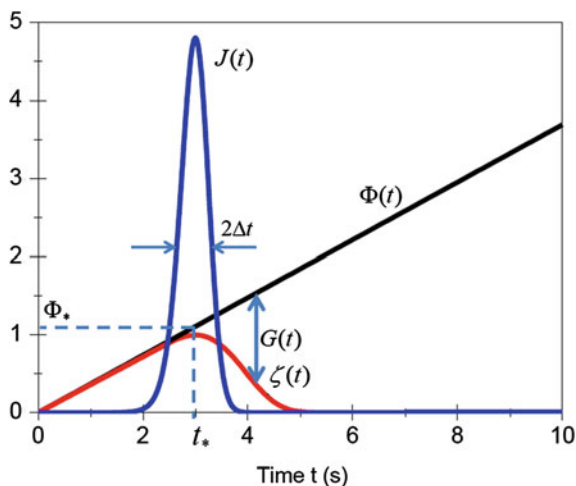
Very importantly, the nucleation rate in (1.205) may become radius-dependent for the following reason. While considering the formation energy in Sect. 1.5, it has always been assumed that an infinitely large metastable phase is not affected by nucleation of a very small particle. This natural assumption becomes irrelevant for nanoparticles. Indeed, when a crystal island nucleates inside or under the nanodroplet, it consumes the growth material from the droplet almost instantaneously, while the refill stage lasts for a much longer time. Depending on the position of the island and the ratio of elementary volumes in the liquid and solid phases, the nucleation may result in changing the droplet volume and consequently its surface area. When such a change occurs, the free energy of island formation ΔG must include the modification of the Laplacian pressure caused by nucleation [82]:

$$\Delta G(i) = -\Delta\mu i + \gamma_{eff} S_{isl} + \gamma \Delta S_L. \quad (1.206)$$

Here, the first two terms are the same as for an infinitely large metastable phase, with $\Delta\mu$ being the difference in chemical potentials between the bulk phases, γ_{eff} the effective surface energy of the island and S_{isl} the island surface area. It should be noticed that the surface energy now depends on the island position. In particular, it is distinctly different for the island entirely surrounded by liquid or replacing some part of the pre-existing liquid–vapor interface by the solid–vapor interface [45]. The position dependence of the formation energy is another interesting feature of nucleation in nano-volumes. The last term in (1.206) thus stands for the modification of a metastable phase itself, where γ is the liquid surface energy and ΔS_L is the change of droplet surface area caused by nucleation. Clearly, this contribution is proportional to $1/R$ and therefore modifies the surface energy term. Our simple considerations show that, while a complex story of modeling the size distribution is absent for just one island emerging in the mononuclear regime, relevant modifications of the formation energy are required for the correct determination of the nucleation probability. This will be further developed in Chaps. 4–6 in connection with the growth mechanisms of semiconductor nanowires.

When the volume of metastable phase is large enough, the nucleation proceeds in the more usual polynuclear mode. An ensemble of nuclei emerging at different times and growing at different rates should be described by a time-dependent size distribution function. Let us briefly consider the growth stages in this case. To specify the analysis, we adopt the common scenario where the supersaturation is achieved due to a material influx into the system. The influx gradually increases the total number of available monomers. The ideal supersaturation $\Phi(t)$ defined in (1.125) is an increasing function of t , for example, a linear function at a time independent P and zero Q . Since the nucleation process requires reaching a certain threshold (or critical) supersaturation ζ_* , the actual supersaturation $\zeta(t)$ follows $\Phi(t)$ below the threshold, as shown in Fig. 1.31. The time period required to establish the critical supersaturation can be called the incubation time t_* . The critical supersaturation

Fig. 1.31 Qualitative representation of nucleation process under a material influx. Φ_* denotes the ideal supersaturation at time t_* corresponding to the maximum supersaturation ζ_*



is also the maximum supersaturation in a given growth process. The maximum is reached due to the dynamic balance between the monomer influx and their sink caused by nucleation, which starts just before the threshold. The maximum supersaturation corresponds to the maximum nucleation rate and the most representative size in the size distribution (in terms of the invariant size ρ) at the follow-up growth stages.

Since the dependence of the nucleation rate on supersaturation is extremely steep, the nucleation process is enabled only in a very narrow region near the supersaturation maximum and exponentially decreases outside this region (see Fig. 1.31). It might be expected that, in the case of nucleation under the material influx, the nucleation stage is short scale compared to the macroscopic time t_* . This feature, explored in more detail in Chap. 2, is of paramount importance for obtaining the narrow and symmetric size distributions of different self-induced nanoobjects such as nanodroplets, colloidal particles and coherent strained islands in heteroepitaxial systems. It is also clear that the characteristics of this short scale nucleation stage in largest measure determine the observed size distributions. During the entire nucleation stage, the mean size of nuclei remains very small and the normalized total number of monomers in the nuclei $G(t)$ is much smaller than supersaturation.

At $t > t_* + \Delta t$, where $2\Delta t$ is the duration of the nucleation stage, the nucleation rate decreases drastically and the nucleation process is effectively turned off. The nuclei having emerged within the time interval $2\Delta t$ continue growing by consuming monomers which are supplied from the surrounding. The nuclei growth leads to the decrease of supersaturation (usually to zero in the large time limit), as shown in Fig. 1.31. The stage of regular, independent growth of nuclei lasts for time t_R , which is usually much longer than Δt . The maximum of size distribution propagates toward larger sizes, while the size dispersion may change as the nuclei grow. The number of monomers in the nucleus $G(t)$ almost matches $\Phi(t)$ at the asymptotic growth stage. The total number of nuclei remains constant at the regular growth stage.

As supersaturation tends to zero, the critical size defined by (1.68) begins to increase. The next stage of system evolution depends on the character of material influx and the growth rate of nuclei. If the material influx is turned off at a certain time or is slow enough, the critical size reaches the pre-existing size distribution and larger nuclei start growing at the expense of smaller ones. This process, called the Ostwald ripening [3, 86–92], has a major impact on the size spectrum: the number of nuclei is no longer conserved and the distribution dispersion increases much faster than at the regular growth stage. The late and slow Ostwald ripening stage leads to the establishment of a universal asymptotic size distribution [86], as discussed in Chap. 2. When the mean size increases faster than the critical one, the Ostwald ripening process is disabled.

In many dense systems such as vapor-deposited thin films or crystallizing liquid alloys, the independent growth of islands is followed by their direct coalescence. The coalescence process can be liquid-like, where two droplets form one bigger droplet of the same shape, or solid-like, leading to the formation of a complex “mosaic” crystal structure. The latter can no longer be described in terms of the number and size of nuclei. Special geometrical and probabilistic approaches should be used at the coalescence stage, treating the crystallizing system in terms of the mean filling factor, surface area or perimeter of crystalline boundaries and so on. In the case of solid-like coalescence, a very useful approach is based on the so-called Kolmogorov–Johnson–Mehl–Avrami crystallization model [93–96]. This model, discussed in detail in Chap. 2, is of great importance in modeling the growth of thin solid films, semiconductor nanowires and many other crystals [65, 80, 97–100].

Main stages of nucleation-condensation process in the case of 2D thin film are shown schematically in Fig. 1.32. As discussed in more detail in Chap. 2, the Ostwald ripening stage is disabled, for example, in the case of 2D islands growing under a constant deposition rate, regardless of their growth mechanism. In this case, the time scale hierarchy of different growth stages is given by

$$t_s \ll 2\Delta t \ll t_R \ll t_c. \quad (1.207)$$

The shortest stage is establishing the stationary state in the near-critical region of sizes, followed by the nucleation stage with the duration $2\Delta t$, then the regular growth with the characteristic time t_R , which is much shorter than the coalescence time t_c at which the islands start touching each other. For example, at the deposition rate of 0.1 ML/s and a small effective desorption rate, the total time required to form a complete monolayer is 10 s, while the coalescence process starts roughly at 5 s, the moment when the film starts reaching continuity.

The size distribution established at the nucleation stage will be studied in detail in Chap. 2. While the particular spectrum shape is not known by this end, some useful information regarding the growth law can be deduced under the assumption that the distribution width is much smaller than the mean size. In open systems, this important property is usually ensured by the shortness of nucleation stage under the material influx, as shown in Fig. 1.31. Taking the example of 2D islands growing in the ballistic regime, the invariant size defined by (1.117) and (1.118) is the island

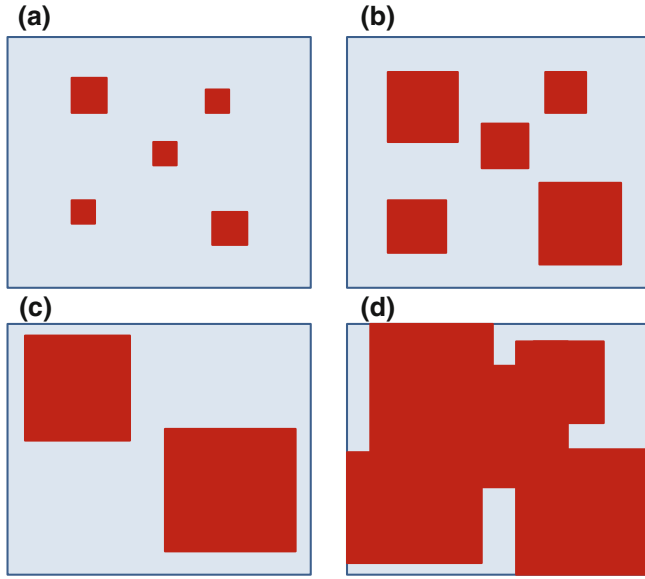


Fig. 1.32 A part of substrate surface containing 5 square islands upon the completion of nucleation stage (a). The islands then grow independently at the regular growth stage (b). If the deposition flux is turned off at a certain time, the Ostwald ripening is observed, where larger islands grow at the expense of smaller ones (c). If the flux remains on, the islands coalesce into a continuous film (d)

radius in the units of lattice spacing, $\rho = i^{1/2}$. We assume that the size distribution in terms of ρ variable is narrow. For example, it can be approximated by the Gaussian

$$f(\rho, z) = \frac{N}{\sqrt{2\pi}\psi(z)} \exp\left[-\frac{(\rho - z)^2}{2\psi(z)}\right], \quad (1.208)$$

in which $z(t) \equiv \rho_*(t)$ is the time-dependent mean size, N is the surface density of islands upon the completion of nucleation stage and $\sqrt{2\psi(z)}/z \ll 1$ during the entire growth stage. In this case, we can use the δ -like approximation for the distribution function in the equation for the total number of adatoms in the islands:

$$G(t) = \frac{1}{n_{1e}} \int_0^\infty d\rho \rho^2 f(z, \rho) \cong \frac{N}{n_{1e}} z^2(t). \quad (1.209)$$

On the other hand, the growth rate of the mean size is given by (1.118):

$$\frac{dz}{dt} = \frac{\zeta}{\tau}. \quad (1.210)$$

The ideal supersaturation in the case of vapor deposition with the time-independent arrival rate χI and the desorption time τ_A is determined by

$$\Phi(t) = \frac{1}{n_{1e}} \int_{t_e}^t dt' \left[\chi I - \frac{n_1(t')}{\tau_A} \right] \cong \Phi_* + \Phi_{\max} \frac{(t - t_*)}{\tau_A} - \frac{\tau}{\tau_A} z(t), \quad t \geq t_* \quad (1.211)$$

Here, $\Phi_{\max} = (\chi I \tau_A)/n_{1e} - 1$ is the maximum ideal supersaturation that would be reached on the surface in absence of nucleation. In the last expression, we assume that ζ equals Φ_* at $t = t_*$, where the time moment t_* corresponds to the supersaturation maximum as shown in Fig. 1.31. This happens when the deposition flux is large enough, that is, at $\Phi_{\max} \gg 1$. Using (1.209–1.211) in the material balance condition $\Phi(t) = \zeta(t) + G(t)$, and assuming that the mean size equals zero at $t = t_*$, we arrive at the closed equation for $z(t)$:

$$\tau \frac{dz}{dt} + \frac{N}{n_{1e}} z^2 + \frac{\tau}{\tau_A} z = \Phi_* + \frac{\Phi_{\max}}{\tau_A} (t - t_*); \quad z(t = t_*) = 0. \quad (1.212)$$

Upon several straightforward substitutions of variables, this non-linear growth equation can be reduced to the linear second order equation for the Airy functions, yielding the exact solution in the form

$$z(t) = [U(x(t)) - \delta] z_0. \quad (1.213)$$

The parameters are defined as follows

$$z_0 \equiv \left(\frac{n_{1e}}{N} \right)^{2/3} \left(\frac{\tau}{\tau_A} \Phi_{\max} \right)^{1/3}; \quad (1.214)$$

$$\delta \equiv \frac{1}{2} \frac{\Phi_*^2}{\Phi_{\max}^{5/3}} \left(\frac{\tau}{\tau_A} \right)^{2/3} \left(\frac{n_{1e}}{N} \right)^{1/3}. \quad (1.215)$$

The function $U(x)$ is given by the ratio of linear combinations of Airy functions and their derivatives

$$U(x) = \frac{Bi'(x) - k |Ai'(x)|}{Bi(x) + k Ai(x)}; \quad k \equiv \frac{Bi'(x_0) - \delta Bi(x_0)}{|Ai'(x_0)| + \delta Ai(x_0)}, \quad (1.216)$$

where $Ai(x)$ is the decreasing and $Bi(x)$ is the increasing Airy function in standard notations [101]. The variable x is the linear function of time

$$x(t) = \beta \left(1 + \nu + \frac{\Phi_{\max}}{\Phi_*} \frac{(t - t_*)}{\tau_A} \right) \quad (1.217)$$

with coefficients

$$\beta = \frac{\Phi_*}{\Phi_{\max}^{2/3}} \left(\frac{\tau_A}{\tau} \right)^{2/3} \left(\frac{N}{n_{1e}} \right)^{1/3}; \quad (1.218)$$

$$\nu = \frac{1}{4} \frac{\Phi_*^5}{\Phi_{\max}^4} \frac{n_{1e}}{N} \left(\frac{\tau}{\tau_A} \right)^2. \quad (1.219)$$

The quantity x_0 in the second (1.216) is defined as $x_0 = x(t = t_*) = \beta(1 + \nu)$.

This solution describes the time evolution of the mean size of surface islands at the known N , Φ_* and t_* , which values are defined at the nucleation stage. The typical dependence of $r_*(t) = \sqrt{\sigma} z(t)/4$ for square islands with side $2r_*$ is shown in Fig. 1.33. The curve is obtained for the parameters approximately corresponding to the Ga-limited growth of GaAs islands on the GaAs(100) substrate at the temperature $T = 580^\circ\text{C}$ with the Ga deposition rate $V = \chi I \sigma \cong I \sigma$ of 0.1 ML/s [102]: $N = 6 \times 10^9 \text{ cm}^{-2}$, $n_{1e} = 3.8 \times 10^{12} \text{ cm}^{-2}$, $\sigma = 0.16 \text{ nm}^2$, $\theta_{1e} = 6 \times 10^{-3}$, $\tau = 3 \times 10^{-3} \text{ s}$, $\tau_A = 2.6 \text{ s}$, $\Phi_{\max} = 42$, $\Phi_* = 1.9$, and $t_* = 0.17 \text{ s}$. It is seen that the mean size increases much faster at the beginning and then reaches the asymptotic regime where z is roughly proportional to $t^{1/2}$.

These features can be understood from the general solution. Indeed, when $(\Phi_{\max} + 1)/(\Phi_* + 1) = n_{1*}/(\chi I \tau_A) \gg 1$, only a tiny fraction of adatoms desorb from the surface (the so-called regime of complete condensation of thin films). The latter inequality is also consistent with $\tau/\tau_A \ll 1$, showing that the islands grow much faster than re-evaporate. Under such conditions, the parameters δ and ν in the above general expressions can be put to zero, while the constant β is larger than 1.5 (it equals 1.62 for the parameters considered). Since $x > \beta$, we can use the known asymptotes of the two Airy functions in (1.216) at large x : $Ai(x) \cong [1/(2\pi^{1/2}x^{1/4})] \exp[-(2x^{3/2})/3]$; $Bi(x) \cong [1/(\pi^{1/2}x^{1/4})] \exp[(2x^{3/2})/3]$. This reduces (1.213) to

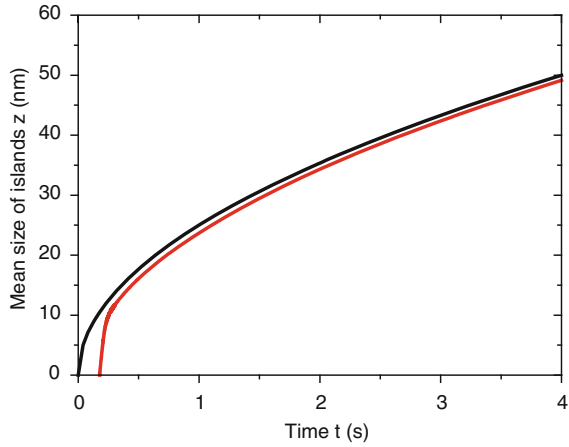
$$z(t) = \sqrt{\frac{\Phi_* \theta_{1e} + (1 - \alpha_{des})V(t - t_*)}{\sigma N}} \tanh \left[C \left(\left(\frac{\Phi_* \theta_{1e} + (1 - \alpha_{des})V(t - t_*)}{\Phi_* \theta_{1e}} \right)^{3/2} - 1 \right) \right] \quad (1.220)$$

with $C \equiv (2/3)\beta^{3/2}$. Here, V is the deposition rate in ML/s, θ_{1e} is the equilibrium adatom coverage at a given temperature and $\alpha_{des} = n_{1e}/(\chi I \tau_A) = \theta_{1e}/(V \tau_A)$ is the small desorption term. The latter equals to only 0.023 in our numerical example. It is seen that the time dependence of mean size is actually expressed via the normalized time $t/t_{ML} = (1 - \alpha_{des})V(t - t_*)$ taking account for both a short waiting time t_* required to reach the maximum adatom supersaturation and a small percentage of desorbed adatoms α_{des} .

Since the constant C is large, the increase of $z(t)$ is faster for shorter times close to t_* . After the relaxation time $\sim 4t_g$, where

$$t_g = \frac{\Phi_* \theta_{1e}}{V} \cong \frac{\Phi_*}{\Phi_{\max}} \tau_A, \quad (1.221)$$

Fig. 1.33 Mean size of 2D square islands obtained with the parameters described in the text from the general (1.213) to (1.219) (red line) and the simplified formula (1.222) (black line)



the mean size given by (1.220) reaches the asymptotic regime

$$z(t) = \sqrt{\frac{\Phi_* \theta_{1e} + (1 - \alpha_{des})V(t - t_*)}{\sigma N}} \cong \sqrt{\frac{(1 - \alpha_{des})Vt}{\sigma N}}. \quad (1.222)$$

This dependence, also shown in Fig. 1.33, contains only the most important characteristic of nucleation stage: the island density N . In our numerical example, the time t_g equals 0.11 s, so that the asymptotic regime is reached already after ~ 0.5 s after the beginning of deposition. The islands therefore obey the simple growth law given by (1.222) most of the time before they coalesce (we remind that the deposition time of 1 ML equals 10 s in our example).

Finally, using the “mono-disperse” approximation given by (1.209) at an arbitrary growth index m :

$$G(t) = \frac{1}{n_{1e}} \int_0^\infty d\rho \rho^m f(z, \rho) \cong \frac{N}{n_{1e}} z^m(t), \quad (1.223)$$

we are able to deduce important information about the asymptotic behaviors of the mean size and supersaturation. Let us consider the case with $Q = 0$, and P being a power law function of time, where the ideal supersaturation is given by

$$\Phi(t) = \frac{1}{n_{1e}} \int_0^t dt' P(t') = \left(\frac{t}{t_\infty} \right)^q. \quad (1.224)$$

Here, q is the flux index and t_∞ is the characteristic macroscopic time required to reach the equilibrium vapor concentration n_{1e} . For example, at $P(t) = I = \text{const}$, $t_\infty = n_{1e}/I = \theta_{1e}/V$ is the time of establishing the equilibrium adatom coverage at a given deposition rate V with neglect of desorption. Writing the material balance given by (1.176) in the form

$$\left(\frac{t}{t_\infty}\right)^q = \zeta(t) + \frac{N}{n_{1e}} z^m(t) \quad (1.225)$$

and assuming that $\zeta \rightarrow 0$ at the asymptotic growth stage, the leading power law asymptote of the mean invariant size is obtained as

$$z(t) = \left(\frac{n_{1e}}{N}\right)^{1/m} \left(\frac{t}{t_\infty}\right)^{q/m}. \quad (1.226)$$

Equation (1.222) is the particular case of (1.226) at $m = 2$ and $q = 1$. Obviously, the supersaturation $\zeta(t) = \tau(dz/dt)$ asymptotically decreases to zero only if $q/m < 1$. Under a constant material influx corresponding to $q = 1$, this happens for all $m > 1$, while the growth at $m = 1$ leads to a constant value of supersaturation in the large time limit. Obviously, such a behavior disables the Ostwald ripening process at $m = 1$ under a material influx.

Nucleation Theory and Growth of Nanostructures

Dubrovskii, V.G.

2014, XIII, 601 p. 358 illus., 126 illus. in color.,

Hardcover

ISBN: 978-3-642-39659-5